Journal of Fluid Mechanics
http://journals.cambridge.org/FLM

Additional services for ***Journal of Fluid Mechanics:***

Email alerts: Click here
Subscriptions: Click here
Commercial reprints: Click here
Terms of use : Click here

Natural convection and the evolution of a reactive porous medium

LINDSEY T. RITCHIE and DAVID PRITCHARD

Journal of Fluid Mechanics / Volume 673 / April 2011, pp 286 - 317
DOI: 10.1017/S0022112010006269, Published online: 17 February 2011

Link to this article: http://journals.cambridge.org/abstract_S0022112010006269

How to cite this article:
LINDSEY T. RITCHIE and DAVID PRITCHARD (2011). Natural convection and the evolution of a reactive porous medium. Journal of Fluid Mechanics, 673, pp 286-317 doi:10.1017/S0022112010006269

Request Permissions : Click here

CAMBRIDGE JOURNALS

Downloaded from http://journals.cambridge.org/FLM, IP address: 130.159.82.152 on 19 Sep 2012

J. Fluid Mech. (2011), *vol.* 673, *pp.* 286–317. © Cambridge University Press 2011
doi:10.1017/S0022112010006269

Natural convection and the evolution of a reactive porous medium

LINDSEY T. RITCHIE† AND DAVID PRITCHARD

Department of Mathematics and Statistics, University of Strathclyde, 26 Richmond Street, Glasgow G1 1XH, Scotland, UK

(Received 29 September 2010; revised 30 November 2010; accepted 1 December 2010; first published online 17 February 2011)

We describe a mathematical model of buoyancy-driven flow and solute transport in a saturated porous medium, the porosity and permeability of which evolve through precipitation and dissolution as a mineral is lost or gained from the pore fluid. Imposing a vertically varying equilibrium solubility creates a density gradient which can drive convective circulation. We characterise the onset of convection using linear stability analysis, and explore the further development of the coupled reaction–convection system numerically. At low Rayleigh numbers, the effect of the reaction–permeability feedback is shown to be destabilising through a novel reaction–diffusion mechanism; at higher Rayleigh numbers, the precipitation and dissolution have a stabilising effect. Over longer time scales, reaction–permeability feedback triggers secondary instabilities in quasi-steady convective circulation, leading to rapid reversals in the direction of circulation. Over very long time scales, characteristic patterns of porosity emerge, including horizontal layering as well as the development of vertical chimneys of enhanced porosity. We discuss the implications of these findings for more comprehensive models of reactive convection in porous media.

Key words: convection in porous media, geophysical and geological flows

1. Introduction

The circulation of fluid through porous rock, under the influence of buoyancy forces associated with thermal or solutal gradients, is believed to occur in many geological settings (Phillips 1991, 2009; Nield & Bejan 2006), although it has been directly observed only occasionally (e.g. Stevens *et al.* 2009). Such fluid generally contains a rich cocktail of dissolved minerals: as the temperature, pressure and local rock chemistry change, the solubilities of these minerals also change and they may be precipitated onto or dissolved from the rock matrix. The role of such processes in controlling the structure of rocks and the characteristic patterns of mineral deposition is still not fully understood.

The theoretical study of convection in a porous medium dates back to the stability analyses of Horton & Rogers (1945) and Lapwood (1948). It is similar to the pure-fluid convection problem first investigated by Bénard and Rayleigh in the early 20th century, but it has some distinctive features. In particular, the presence of a porous matrix allows dissolved chemical species to be lost or gained by the fluid throughout the medium, instead of merely at the boundaries. Therefore, the models

† Email address for correspondence: lindsey.ritchie@strath.ac.uk

developed to describe reactive convection in a porous medium (e.g. Steinberg & Brand 1983, 1984; Gatica, Viljoen & Hlavacek 1989; Viljoen, Gatica & Hlavacek 1990; Pritchard & Richardson 2007) can exhibit different mathematical behaviour from those developed to describe reactive convection in a pure fluid layer (e.g. Bdzil & Frisch 1971, 1980; Wollkind & Frisch 1971; Gutkowicz-Krusin & Ross 1980). Apart from the mathematical interest of these models, they also have a range of applications in environmental and geological fluid dynamics. These include the dolomitisation of carbonate platforms (Kaufman 1994), soil salinisation (Gilman & Bear 1994; Wooding, Tyler & White 1997), heat transfer in geothermal reservoirs (Oldenburg & Pruess 1998) and the formation of uranium ore deposits (Raffensperger & Garven 1995*a*,*b*).

A particular feature of reactive flow in a porous medium, including convective flow, is the possibility of feedback as the exchange of minerals alters the permeability of the medium, which in turn alters the patterns of flow: inhomogeneous permeability may even control whether large-scale flow is able to occur (Sharp & Shi 2009). A general discussion of flow–reaction feedback has been presented by Phillips (1991, 2009), and some specific problems have received particular interest. Perhaps the most thoroughly studied topic is the 'reaction–infiltration' or 'wormholing' instability (see e.g. Chadam *et al.* 1986; Hinch & Bhatt 1990; Chadam *et al.* 2001; Zhao *et al.* 2008). In this process, a dissolution front moving through a porous medium undergoes fingering as the flow focuses into relatively permeable channels, further dissolving the medium in these channels and thus enhancing their permeability still further. Other flow–reaction processes that have received attention from modellers include the self-sealing of fractures in hydrothermal upflow zones (Lowell, Cappellen & Germanovitch 1993), the propagation of gravity currents through a reactive medium (Raw & Woods 2003; Verdon & Woods 2007), the dynamics and thermodynamics of magma chambers (Hallworth, Huppert & Woods 2005), the cementation of sandstones (Cochepin *et al.* 2008), and, in recent years, the geochemical sequestration of carbon dioxide (Ennis-King & Paterson 2007). There are also some parallels to be drawn with the behaviour of mushy layers (Worster 1997), although the model we will consider differs in some key respects from that of an ideal mushy layer: we will discuss this further in § 2.

The possibility that convective fluid circulation in geological formations might experience flow–reaction–permeability feedback has received relatively little attention from mathematical modellers. An exception is the work of Bolton, Lasaga & Rye (1996, 1997, 1999), who constructed a detailed mathematical model of buoyancy-driven flow in a quartz–silicic acid system. Their main interest was in how reaction–convection feedback modified rocks with pre-existing permeability structures, such as fracture zones and fault zones. They found extremely complicated patterns of coupled flow and transport, in which both thermosolutal effects and the finite time scale associated with reactions appeared to be important.

While models as complicated as those of Bolton *et al.* are undoubtedly required to describe real geological systems, there is also a case for studying more heavily idealised models to identify the key mechanisms and interactions involved in reactive convection. This was the approach taken by Pritchard & Richardson (2007) in a precursor to the present study, which investigated the effect of a thermally controlled reaction on thermosolutal convection in a porous layer and concluded that it could have significant consequences for the onset of convection. Although Pritchard & Richardson (2007) noted the possibility of long-term changes to the porous medium as a result of this convection, they did not pursue the point further. The present study represents a first step in this direction.

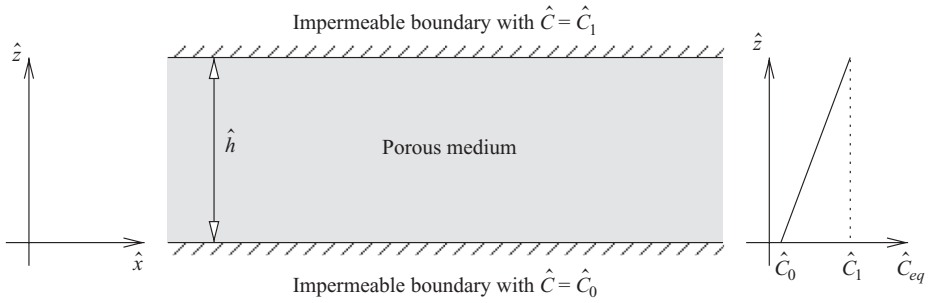

FIGURE 1. Schematic diagram of the system under consideration.

We consider the simplest model in which reaction–convection interactions may occur: convection driven solely by solutally induced density effects, in which dissolution and precipitation act to restore the local solute concentration to some local equilibrium value that varies with depth in the medium. This is a simple model of thermally controlled solubility in a system in which rapid thermal diffusion preserves a uniform geothermal temperature gradient; perhaps less realistically, it could also be interpreted as representing vertically varying mineralogy. We reiterate, however, that it is intended as an idealisation and not as a detailed geochemical model of any particular system.

In § 2 we present a model of flow and transport in a porous medium with evolving porosity. We then, in § 3, carry out a linear stability analysis of the onset of convection, paying particular attention to the permeability feedback effects which enter on a longer time scale than that of the flow. In § 4, we validate the stability analysis using a numerical model and carry out a sequence of numerical experiments to investigate the longer-term behaviour of the system. In particular, we seek to identify and interpret particular feedback mechanisms which control the evolution of the porous matrix. Finally, in § 5 we summarise our results and draw some general conclusions.

2. Model description

We consider an initially homogeneous and isotropic porous layer of depth $\hat{h}$ with solutal mass concentrations $\hat{C}_0$ and $\hat{C}_1$ imposed at the bottom and top, respectively (figure 1). The bottom and top layers are presumed to be impermeable, and we impose chemical equilibrium at the boundaries.

We take $\hat{x}$ and $\hat{z}$ as the horizontal and vertical coordinates, respectively, with $\hat{z}$ increasing upwards. Making a Boussinesq approximation, the flow is governed by the equations of mass conservation and Darcy's law (Phillips 1991, §§ 2.5 and 2.6),

$$\frac{\partial \phi}{\partial \hat{t}} + \hat{\nabla} \cdot \hat{\boldsymbol{u}} = 0, \tag{2.1}$$

$$\hat{\boldsymbol{u}} = -\frac{\hat{K}(\phi)}{\hat{\mu}} \hat{\nabla} \hat{p} - \frac{\hat{K}(\phi)}{\hat{\mu}} \hat{\rho}_f(\hat{C}) \hat{g} \boldsymbol{e}_z, \tag{2.2}$$

where $\hat{K}(\phi)$ is the permeability which depends on the porosity ϕ, $\hat{\mu}$ is the fluid viscosity, $\hat{\rho}_f$ is the fluid density, and $\hat{\boldsymbol{u}}$ is the two-dimensional fluid transport velocity. Throughout this study, a caret will denote a dimensional variable, while dimensionless variables are unadorned.

The permeability $\hat{K}(\phi)$ is given, following Phillips (1991, §4.7), by

$$\hat{K}(\phi) = \hat{K}_0 \left(\frac{\phi}{\phi_0} \right)^b, \tag{2.3}$$

where $\hat{K}_0$ is the initial permeability, ϕ_0 is the initial porosity, and the exponent b typically lies between 2 and 3 inclusive. We will take $b = 2$ throughout.

The transport of solute is described by the advection–diffusion equation

$$\frac{\partial(\phi \hat{C})}{\partial \hat{t}} + \hat{\nabla} \cdot (\hat{\boldsymbol{u}} \hat{C}) = \hat{\nabla} \cdot (\phi \hat{\kappa}_C \hat{\nabla} \hat{C}) + \hat{k}(\phi)(\hat{C}_{eq}(\hat{z}) - \hat{C}). \tag{2.4}$$

Here $\hat{C}$ represents the mass concentration of solute in the fluid, and $\hat{C}_{eq}(\hat{z})$ is the equilibrium concentration of solute, which we assume varies linearly in $\hat{z}$; $\hat{\kappa}_C$ is the molecular diffusivity of the solute through the fluid. Note that the choice of a linearly varying equilibrium concentration will permit us to define a non-evolving diffusive base state for the system.

The reaction rate $\hat{k}(\phi) \geqslant 0$ implicitly depends on the surface area of the rock exposed to the fluid within the pore network. A detailed model of this dependency requires knowledge of the pore-scale geometry and its evolution. As such information is not generally available, we employ the minimal assumption that the reaction rate should reduce to zero when either there is no rock or there are no pores. Therefore, for exploratory purposes we take

$$\hat{k}(\phi) = \hat{k}_{ref} \phi (1 - \phi), \tag{2.5}$$

where $\hat{k}_{ref}$ is some reference reaction rate which we define using the initial porosity ϕ_0 and initial reaction rate $\hat{k}_0$, so

$$\hat{k}_0 = \hat{k}_{ref} \phi_0 (1 - \phi_0). \tag{2.6}$$

The porosity evolution is governed by

$$\frac{\partial \phi}{\partial \hat{t}} = \frac{\hat{k}(\phi)}{\hat{\rho}_s} (\hat{C}_{eq}(\hat{z}) - \hat{C}), \tag{2.7}$$

where $\hat{\rho}_s$ is the solid matrix density. Equations (2.5)–(2.7) are of a similar form to those used in the study of dissolution fronts in fluid-saturated porous media (Chadam *et al.* 1986, 2001; Zhao *et al.* 2008). As these studies demonstrate, different forms for the dependence of reaction rate on porosity could readily be employed but have not been shown to be of critical importance.

Finally, we take the density to be given by the linear approximation

$$\hat{\rho}_f(\hat{C}) = \hat{\rho}_0 [1 + \hat{\beta}_C (\hat{C} - \hat{C}_0)]. \tag{2.8}$$

We seek a steady-state base solution in which $\hat{\boldsymbol{u}} = 0$ and there is no lateral variation. We then find a linear distribution of solute concentration,

$$\hat{C}_s(\hat{z}) = \hat{C}_0 + (\hat{C}_1 - \hat{C}_0) \frac{\hat{z}}{\hat{h}} = \hat{C}_{eq}(\hat{z}). \tag{2.9}$$

Some key differences between this model and that of convective flow in an ideal mushy layer (Worster 1997) should be noted at this point. The most obvious difference is the boundary conditions, as mushy layers are typically bounded between pure solid and liquid phases; other differences include the relative insignificance of latent heat,

the inclusion of solutal diffusion, and the dependence of reaction rate on porosity which arises because the reaction involves the direct exchange of solute with the solid matrix. Furthermore, in the mushy-layer problem a thermodynamic constraint links the thermal and solute fields, whereas since we consider a system with a fixed temperature gradient, the thermal field is effectively decoupled from the dynamics. Thus, although we may expect loose analogies with mushy-layer convection, we may also expect distinct behaviour in the present model.

2.1. *Non-dimensionalisation*

Equation (2.4) may be simplified using (2.1) to obtain

$$\phi\frac{\partial\hat{C}}{\partial\hat{t}}+(\hat{\boldsymbol{u}}\cdot\hat{\nabla})\hat{C}=\hat{\kappa}_C\hat{\nabla}\cdot(\phi\hat{\nabla}\hat{C})+\hat{k}(\phi)(\hat{C}_{eq}(\hat{z})-\hat{C}). \tag{2.10}$$

A further simplification, following most previous workers on the subject (e.g. Bolton *et al.* 1999; Phillips 2009), is to neglect the time derivative in (2.1). This is valuable because it permits the use of a streamfunction formulation for velocity. It is straightforward, although laborious, to show that this affects the linear stability of the system only at order δ^2, where $\delta\ll 1$ is defined below.

We now define dimensionless variables as

$$\hat{\boldsymbol{x}}=\hat{h}\boldsymbol{x},\quad \hat{\boldsymbol{u}}=\frac{\hat{\kappa}_C}{\hat{h}}\boldsymbol{u},\quad \hat{t}=\frac{\phi_0\hat{h}^2}{\hat{\kappa}_C}t,\quad \hat{p}=\frac{\hat{\kappa}_C\hat{\mu}}{\hat{K}_0}p,\quad \hat{C}=\hat{C}_0+(\hat{C}_1-\hat{C}_0)C, \tag{2.11}$$

to obtain the dimensionless governing equations

$$\nabla\cdot\boldsymbol{u}=0, \tag{2.12}$$

$$\nabla p=-\left(\frac{\phi}{\phi_0}\right)^{-b}\boldsymbol{u}-\mathscr{R}_C C\boldsymbol{e}_z-\frac{\mathscr{R}_C}{\hat{\beta}_C(\hat{C}_1-\hat{C}_0)}\boldsymbol{e}_z, \tag{2.13}$$

$$\frac{\phi}{\phi_0}\frac{\partial C}{\partial t}+(\boldsymbol{u}\cdot\nabla)C=\nabla\cdot(\phi\nabla C)-k_0\frac{\phi(1-\phi)}{\phi_0(1-\phi_0)}(C-z), \tag{2.14}$$

$$\frac{\partial\phi}{\partial t}=-\delta k_0\frac{\phi(1-\phi)}{1-\phi_0}(C-z), \tag{2.15}$$

with the boundary conditions

$$w=0\quad\text{and}\quad C=z\quad\text{at}\quad z=0\quad\text{and}\quad z=1. \tag{2.16}$$

The dimensionless parameters k_0, δ and $\mathscr{R}_C$ are defined, respectively, as

$$k_0=\frac{\hat{h}^2\hat{k}_0}{\hat{\kappa}_C},\qquad \delta=\frac{(\hat{C}_1-\hat{C}_0)}{\hat{\rho}_s},\qquad \mathscr{R}_C=\frac{\hat{K}_0\hat{\rho}_0\hat{g}\hat{h}\hat{\beta}_C(\hat{C}_1-\hat{C}_0)}{\hat{\mu}\hat{\kappa}_C}. \tag{2.17}$$

The parameter $\mathscr{R}_C$ is a solutal Rayleigh number, positive values of which correspond to an unstable solutal density gradient. The parameter $k_0>0$ is a Damköhler number which provides the dimensionless reaction rate for the system: note that estimates for geochemical reaction rates may vary by many orders of magnitude (Phillips 2009, § 2.8). Finally, δ is a matrix evolution rate, which may be assumed to be much less than unity since mass concentrations of solute are typically much smaller than the density of the solid mineral (Phillips 2009, § 2.8).

3. Linear stability analysis

We define infinitesimal perturbation variables, denoted by a dash, as

$$\boldsymbol{u}' = \boldsymbol{u}, \quad C' = C - z, \quad p' = p + \frac{1}{2}\mathscr{R}_C z^2 + \frac{\mathscr{R}_C}{\hat{\beta}_C(\hat{C}_1 - \hat{C}_0)}z, \quad \phi' = \phi - \phi_0. \tag{3.1}$$

By neglecting second-order quantities, we may simplify (2.12)–(2.15) to obtain

$$\nabla \cdot \boldsymbol{u}' = 0, \tag{3.2}$$

$$\nabla p' = -\boldsymbol{u}' - \mathscr{R}_C C' \boldsymbol{e}_z, \tag{3.3}$$

$$\frac{\partial C'}{\partial t} + w' = \phi_0 \nabla^2 C' + \frac{\partial \phi'}{\partial z} - k_0 C', \tag{3.4}$$

$$\frac{\partial \phi'}{\partial t} = -\delta k_0 \phi_0 C'. \tag{3.5}$$

The boundary conditions are given by

$$w' = 0 \quad \text{and} \quad C' = 0 \quad \text{at} \quad z = 0 \quad \text{and} \quad z = 1. \tag{3.6}$$

We seek solutions of the form

$$\left.\begin{aligned} u' &= U(z)\mathrm{e}^{\mathrm{i}mx}\mathrm{e}^{\sigma t}, \quad w' = W(z)\mathrm{e}^{\mathrm{i}mx}\mathrm{e}^{\sigma t}, \quad p' = P(z)\mathrm{e}^{\mathrm{i}mx}\mathrm{e}^{\sigma t}, \\ C' &= \chi(z)\mathrm{e}^{\mathrm{i}mx}\mathrm{e}^{\sigma t}, \quad \phi' = \Phi(z)\mathrm{e}^{\mathrm{i}mx}\mathrm{e}^{\sigma t}, \end{aligned}\right\} \tag{3.7}$$

where the real parts are assumed, the wavenumber m is a positive real number, and U, W, P, χ, Φ and σ are generally complex. Substituting these into (3.2)–(3.5), we obtain

$$\mathrm{i}mU(z) + \frac{\mathrm{d}}{\mathrm{d}z}W(z) = 0, \tag{3.8}$$

$$\mathrm{i}mP(z) = -U(z), \tag{3.9}$$

$$\frac{\mathrm{d}}{\mathrm{d}z}P(z) = -W(z) - \mathscr{R}_C \chi(z), \tag{3.10}$$

$$\left[\phi_0\left(\frac{\mathrm{d}^2}{\mathrm{d}z^2} - m^2\right) - k_0 - \sigma\right]\chi(z) = W(z) - \frac{\mathrm{d}}{\mathrm{d}z}\Phi(z), \tag{3.11}$$

$$\sigma\Phi(z) = -\delta k_0 \phi_0 \chi(z). \tag{3.12}$$

Equations (3.8)–(3.12) can be combined and simplified to give

$$\left[\phi_0\left(\frac{\mathrm{d}^2}{\mathrm{d}z^2} - m^2\right) - \frac{\delta k_0 \phi_0}{\sigma}\frac{\mathrm{d}}{\mathrm{d}z} - (k_0 + \sigma)\right]\left[\frac{\mathrm{d}^2}{\mathrm{d}z^2} - m^2\right]W(z) = m^2 \mathscr{R}_C W(z), \tag{3.13}$$

while $W(z)$ must satisfy the boundary conditions

$$W(z) = 0 \quad \text{and} \quad \left(\frac{\mathrm{d}^2}{\mathrm{d}z^2} - m^2\right)W(z) = 0 \quad \text{at} \quad z = 0 \quad \text{and} \quad z = 1. \tag{3.14}$$

Adapting the approach of Chandrasekhar (1961, § 15) for Rayleigh–Bénard convection, we seek solutions to (3.13) in the form $W(z) \propto \exp(qz)$, where q is a root of the auxiliary equation

$$\left[\phi_0(q^2 - m^2) - \frac{\delta k_0 \phi_0}{\sigma}q - (k_0 + \sigma)\right][q^2 - m^2] = m^2 \mathscr{R}_C. \tag{3.15}$$

In general, we may write

$$W(z) = A_1 \mathrm{e}^{q_1 z} + A_2 \mathrm{e}^{q_2 z} + A_3 \mathrm{e}^{q_3 z} + A_4 \mathrm{e}^{q_4 z}, \tag{3.16}$$

and the boundary conditions (3.14) may be written as

$$B\cdot\begin{bmatrix}A_1\\A_2\\A_3\\A_4\end{bmatrix}=\mathbf{0},\quad\text{where}\quad B=\begin{bmatrix}1 & 1 & 1 & 1\\ \mathrm{e}^{q_1} & \mathrm{e}^{q_2} & \mathrm{e}^{q_3} & \mathrm{e}^{q_4}\\ (q_1^2-m^2) & (q_2^2-m^2) & (q_3^2-m^2) & (q_4^2-m^2)\\ (q_1^2-m^2)\mathrm{e}^{q_1} & (q_2^2-m^2)\mathrm{e}^{q_2} & (q_3^2-m^2)\mathrm{e}^{q_3} & (q_4^2-m^2)\mathrm{e}^{q_4}\end{bmatrix}. \tag{3.17}$$

For non-trivial solutions, therefore, we require that

$$\det(B)=0. \tag{3.18}$$

3.1. *Reaction but no matrix evolution*

Before considering the full linear stability problem, it is helpful to examine the rather simpler case $\delta=0$, so the reaction acts to eliminate solutal perturbations but does not modify the porosity.

If we take $\delta=0$, then the terms in (3.15) that are linear in q disappear, and it has roots $q_1=-q_2$ and $q_3=-q_4=-\mathrm{i}q_0$, where

$$\left.\begin{aligned}q_1&=\left[\frac{1}{2\phi_0}(k_0+\sigma+2\phi_0m^2+\sqrt{(k_0+\sigma)^2+4\phi_0m^2\mathscr{R}_C})\right]^{1/2},\\ q_0&=\left[-\frac{1}{2\phi_0}(k_0+\sigma+2\phi_0m^2-\sqrt{(k_0+\sigma)^2+4\phi_0m^2\mathscr{R}_C})\right]^{1/2}.\end{aligned}\right\} \tag{3.19}$$

The condition (3.18) for non-trivial solutions therefore becomes

$$((k_0+\sigma)^2+4\phi_0m^2\mathscr{R}_C)\sinh(q_1)\sin(q_0)=0. \tag{3.20}$$

For this reduced problem the principle of exchange of stabilities holds (see Appendix A.1), so for marginal stability we set $\sigma=0$. Equation (3.20) then has solutions given by

$$k_0^2+4\phi_0m^2\mathscr{R}_C=0, \tag{3.21}$$

or

$$q_1=\left[\frac{1}{2\phi_0}\left(k_0+2\phi_0m^2+\sqrt{k_0^2+4\phi_0m^2\mathscr{R}_C}\right)\right]^{1/2}=0, \tag{3.22}$$

or

$$q_0=\left[-\frac{1}{2\phi_0}\left(k_0+2\phi_0m^2-\sqrt{k_0^2+4\phi_0m^2\mathscr{R}_C}\right)\right]^{1/2}=n\pi, \tag{3.23}$$

where $n\in\mathbb{Z}$.

It is straightforward to demonstrate that the possibilities (3.21), (3.22) and (3.23) with $n=0$ each give repeated roots in (3.15), and therefore cannot lead to a non-trivial solution of the linear problem. We are left with one remaining possibility:

$$\mathscr{R}_C=\mathscr{R}_{C,0}(m)=\frac{(\phi_0(n^2\pi^2+m^2)+k_0)(n^2\pi^2+m^2)}{m^2}, \tag{3.24}$$

where $n\in\mathbb{Z}$, $n\neq0$, and the four solutions to (3.13) remain linearly independent.

The quantity $\mathscr{R}_{C,0}(m)$ takes its minimum value, $\mathscr{R}_{C,0}^{crit}$, when

$$n = 1 \quad \text{and} \quad m = m_0^{crit} = \pi\left(1 + \frac{k_0}{\pi^2\phi_0}\right)^{1/4}, \tag{3.25}$$

so

$$\mathscr{R}_{C,0}^{crit} = \phi_0\pi^2\left[1 + \left(1 + \frac{k_0}{\pi^2\phi_0}\right)^{1/2} + \frac{k_0}{\pi^2\phi_0}\right]\left[1 + \left(1 + \frac{k_0}{\pi^2\phi_0}\right)^{1/2}\right]\left(1 + \frac{k_0}{\pi^2\phi_0}\right)^{-1/2}. \tag{3.26}$$

If we set $k_0 = 0$ in (3.25) and (3.26), then we recover the marginal stability condition $\mathscr{R}_{C,0}^{crit} = 4\phi_0\pi^2$ for single-diffusive solutal convection in a non-evolving porous medium. Figure 8(a) illustrates how $\mathscr{R}_{C,0}^{crit}$ increases with increasing k_0.

It can be seen from (3.25) and (3.26) that increasing the reaction rate k_0 both stabilises the system (by eliminating destabilising solutal perturbations) and favours the development of narrower convection cells. Pritchard & Richardson (2007) found the same qualitative behaviour in solutally destabilised double-diffusive convection with a reaction term, reflecting the strong similarity between these models. We will discuss below (§ 3.3) how the predictions with $\delta = 0$ relate to the onset of convection in the full system.

3.2. *Linear stability analysis of the full problem*

When $\delta \neq 0$, an analytical solution to (3.18) in terms of σ is not available. Therefore, the stability problem was investigated numerically by a continuation method, tracking σ as $\mathscr{R}_C$ changed, while keeping all other parameters fixed. A numerical solution to (3.20) for a large initial value of $\mathscr{R}_C$ was used as an initial guess. This method was implemented in Maple 12, using the built-in routine `fsolve`.

Unfortunately, the task of tracking the solution branch is numerically very laborious, largely because the analytical solutions for q_i are prohibitively complicated and so nested numerical solutions of (3.15) and (3.18) are required. Additionally, we found that to track a single branch it was necessary to reduce $\mathscr{R}_C$ in steps not larger than 10^{-2}, with smaller steps being required close to the bifurcation point discussed below (§ 3.3). On a desktop computer, the calculation of the results shown in figure 2 required around 2 h to produce. This effectively precluded the thorough investigation of the full problem defined by (3.18); instead, a less formal Galerkin approach was employed both in order to search parameter space and to provide insight into the solution structure.

3.3. *Galerkin approach to the linear stability problem*

In the Galerkin approach, the vertical structure of the perturbations is approximated by a severely truncated Fourier series in z, producing a set of equations that may more readily be solved to provide rapid estimates of the stability behaviour.

3.3.1. *Galerkin approach*

We start with the system (3.8)–(3.12), subject to the boundary conditions

$$\chi = 0 \quad \text{and} \quad W = 0 \quad \text{on} \quad z = 0 \quad \text{and} \quad z = 1, \tag{3.27}$$

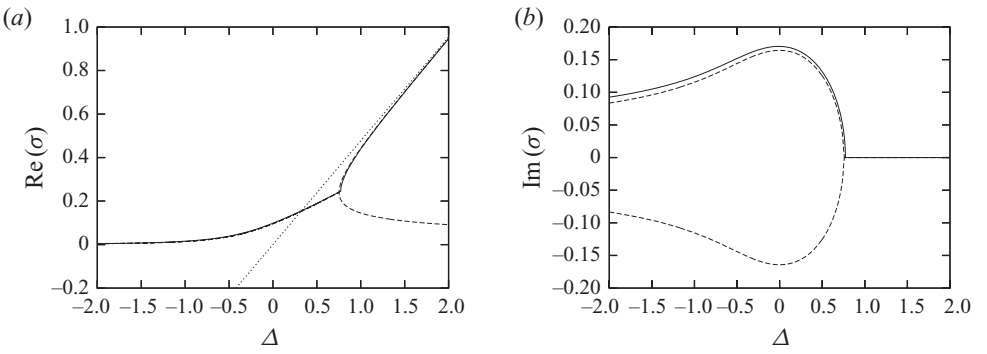

FIGURE 2. Behaviour of σ close to $\Delta = 0$, for $k_0 = 10$, $\delta = 0.1$, $\phi_0 = 0.1$ and $m = 3$. Plot (a) shows Re(σ), while (b) shows Im(σ). Solid lines are full numerical solutions to the linear problem; dashed lines are Galerkin solutions for the upper two roots; dotted line in (a) shows the results for $\delta = 0$.

and to the usual non-triviality condition that the solution is not identically zero. Eliminating U, Φ and P we obtain the system

$$-\frac{1}{m^2}\frac{\mathrm{d}^2 W}{\mathrm{d}z^2} = -W - \mathscr{R}_C \chi, \tag{3.28}$$

$$\phi_0\left(\frac{\mathrm{d}^2\chi}{\mathrm{d}z^2} - m^2\chi\right) - (k_0+\sigma)\chi = W + \frac{\delta k_0 \phi_0}{\sigma}\frac{\mathrm{d}\chi}{\mathrm{d}z}, \tag{3.29}$$

subject to the same boundary conditions. It is possible to further eliminate either χ or W as in (3.13), but as this complicates the boundary conditions we retain both.

We will seek approximate solutions in the form

$$W(z) = \sin(\pi z) + W_2 \sin(2\pi z), \quad \chi(z) = \chi_1 \sin(\pi z) + \chi_2 \sin(2\pi z). \tag{3.30}$$

Note that the boundary conditions are automatically satisfied and the non-triviality condition has been imposed by normalising the $\sin(\pi z)$ component of $W(z)$. We know that in the limit $\delta = 0$ this approximation will become exact, with $W_2 = 0 = \chi_2$; meanwhile, we expect the second harmonics to be the first Fourier mode excited by interactions, as in the study of reactive convection by Gatica *et al.* (1989) and in nonlinear convection problems close to the stability boundary (see e.g. Rudraiah, Srimani & Friedrich 1982; Mamou & Vasseur 1999; Pritchard & Richardson 2007).

With four unknowns, we can choose to satisfy four integral conditions. The natural ones are obtained by extracting the first and second Fourier sine components of (3.28) and (3.29):

$$\int_0^1 \sin(\pi n z)\left[-\frac{1}{m^2}\frac{\mathrm{d}^2 W}{\mathrm{d}z^2}\right]\mathrm{d}z = \int_0^1 \sin(\pi n z)\left[-W - \mathscr{R}_C\chi\right]\mathrm{d}z, \tag{3.31}$$

$$\int_0^1 \sin(\pi n z)\left[\phi_0\left(\frac{\mathrm{d}^2\chi}{\mathrm{d}z^2} - m^2\chi\right) - (k_0+\sigma)\chi\right]\mathrm{d}z = \int_0^1 \sin(\pi n z)\left[W + \frac{\delta k_0\phi_0}{\sigma}\frac{\mathrm{d}\chi}{\mathrm{d}z}\right]\mathrm{d}z, \tag{3.32}$$

for $n=1$ and for $n=2$. This yields a system of four algebraic equations:

$$\frac{\pi^2}{2m^2} = -\frac{1}{2} - \frac{\mathscr{R}_C}{2}\chi_1, \tag{3.33}$$

$$-\frac{1}{2}(\phi_0\pi^2 + \phi_0 m^2 + k_0 + \sigma)\chi_1 = \frac{1}{2} - \frac{4\delta k_0\phi_0}{3\sigma}\chi_2, \tag{3.34}$$

$$\frac{2\pi^2 W_2}{m^2} = -\frac{1}{2}W_2 - \frac{\mathscr{R}_C}{2}\chi_2, \tag{3.35}$$

$$-\left(2\phi_0\pi^2 + \frac{\phi_0 m^2}{2} + \frac{k_0+\sigma}{2}\right)\chi_2 = \frac{1}{2}W_2 + \frac{4\delta k_0\phi_0}{3\sigma}\chi_1. \tag{3.36}$$

The most productive approach to these equations is to eliminate W_2, χ_1 and χ_2 to obtain an equation for σ. Before doing so, it is helpful to express the Rayleigh number in terms of the critical condition for $\delta=0$. We define $\mathscr{R}_C = \mathscr{R}_{C,0}(m) + \Delta$, where $\mathscr{R}_{C,0}(m)$ is given by (3.24). We can now write the growth rate for $\delta=0$ as

$$\sigma = \sigma_0 = \frac{m^2\Delta}{\pi^2 + m^2}. \tag{3.37}$$

With this notation, we find that $\sigma \neq 0$ satisfies the quartic

$$a_4\sigma^4 + a_3\sigma^3 + a_2\sigma^2 + a_1\sigma + a_0 = 0, \tag{3.38}$$

where

$$a_4 = 9m^4 + 36\pi^4 + 45\pi^2 m^2, \tag{3.39}$$

$$a_3 = 27\pi^2 k_0(m^2+\pi^2) + 54\pi^2\phi_0 m^4 + 189\pi^4\phi_0 m^2 + 135\pi^6\phi_0 - (18m^4 + 45\pi^2 m^2)\Delta, \tag{3.40}$$

$$a_2 = -(135\pi^4\phi_0 m^2 + 54\pi^2\phi_0 m^4 + 27\pi^2 k_0 m^2)\Delta + 9m^4\Delta^2, \tag{3.41}$$

$$a_1 = 0, \tag{3.42}$$

$$a_0 = (256\pi^4 + 320\pi^2 m^2 + 64m^4)\phi_0^2 k_0^2\delta^2. \tag{3.43}$$

Because (3.38) is a polynomial, it is straightforward to locate all the complex roots numerically (for example, using the `fsolve` command in Maple), and thus to track all the solutions through parameter space.

3.3.2. *The behaviour of roots* $\sigma(\mathscr{R}_C; m)$

Figure 2 shows representative results when the wavenumber m and all the parameters except Δ are fixed, while Δ is varied about zero. For this, and all subsequent figures in this section, the default parameter values were $\phi_0 = 0.1$, $k_0 = 10$ and $\delta = 0.1$; this rather large value of δ was chosen to make deviations from the case $\delta = 0$ as apparent as possible.

When Δ is large and positive, so $\mathscr{R}_C$ is somewhat larger than $\mathscr{R}_{C,0}$, the branch of σ with largest real part closely tracks σ_0. It deviates weakly from this as Δ is reduced, until this branch and the one below merge. This occurs at about $\Delta \approx 0.7$ in figures 2(*a*) and 2(*b*); more generally (see the asymptotic analysis in § A.2.1), the point at which this occurs scales as $\Delta \sim \delta^{2/3}$ and $\sigma \sim \delta^{2/3}$. At this bifurcation point, the values of σ become complex. As Δ is further reduced, $\mathrm{Re}(\sigma)$ continues to fall, but never reaches zero, asymptoting towards it as $\Delta \to -\infty$ (see § A.2.3); meanwhile $\mathrm{Im}(\sigma)$ first increases rapidly in magnitude and then decays. This behaviour appears to be generic for all values of m, although the position of the bifurcation point changes with m.

This behaviour may be interpreted physically. It is straightforward to show from (3.8)–(3.12) that the principle of the exchange of stabilities does not hold for the base state, since when $\sigma = 0$ and $\delta \neq 0$, (3.12) requires $\chi = 0$, and the system may be reduced to $\mathrm{d}^2W/\mathrm{d}z^2 = m^2W$ with $W(0) = 0 = W(1)$ and no non-trivial solutions. Thus, although the system with $\delta \neq 0$ can mimic the system with $\delta = 0$ closely (to within $\mathcal{O}(\delta^2)$: see § A.2.2), as $\mathscr{R}_C \to \mathscr{R}_{C,0}$ something must break down. What emerges is a weakly growing travelling mode, which will be discussed further in the next section. It is interesting and unexpected that the system remains faintly unstable even when $\mathscr{R}_C$ is reduced well below $\mathscr{R}_{C,0}$.

Figure 2 also compares the predictions of the Galerkin analysis with those from the full numerical solution of (3.18), again taking a relatively large value of δ. Good agreement can be seen for values of Δ as low as the bifurcation point; even thereafter, the real part of the growth rate is tracked very accurately, while errors in the imaginary part are of the order of 10 %. Further comparisons were carried out for smaller values of δ, with correspondingly still better agreement. Note that the numerical solution tracks only one branch below the bifurcation point, and it appears to be arbitrary whether it selects the positive or the negative solution for $\mathrm{Im}(\sigma)$.

3.3.3. *Eigenfunction structure and instability mechanism*

The Galerkin stability analysis provides not just the complex growth rate σ but also the quantities W_2, χ_1 and χ_2 that define the corresponding vertical eigenfunction. To elucidate the mechanism involved in the instability, it is useful to examine these quantities.

Note first that, in contrast to the situation in non-reactive double-diffusive convection where complex conjugate growth rates appear, the two complex conjugate solutions here have different vertical structures. This means that rather than taking the form of a stationary amplifying oscillation, the instability here can take the form of an amplifying travelling wave.

It is useful first to identify how the second harmonic alters the shapes and relative phases of the various perturbations. We may write

$$\begin{aligned} w(x, z, t) &= \mathrm{Re}\left(\mathrm{e}^{\mathrm{i}mx}\mathrm{e}^{(\sigma_R + \mathrm{i}\sigma_I)t}(\sin(\pi z) + W_2 \sin(2\pi z))\right) \\ &= \mathrm{e}^{\sigma_R t}[\sin(\pi z)\cos(mx + \sigma_I t) + |W_2| \sin(2\pi z)\cos(mx + \sigma_I t + \theta)], \end{aligned} \tag{3.44}$$

where $\theta = \arg(W_2)$. It is clear that $|W_2|$ controls the relative strength of the second harmonic. The relative phase θ then controls the way in which the second harmonic distorts the first. If $\theta = 0$, then the second harmonic accentuates the perturbation in $0 < z < 1/2$ and reduces it in $1/2 < z < 1$: the net effect is to distort the convection cells by squashing them downwards towards the base of the layer. Similarly, if $\theta = \pm\pi$, the second harmonic squashes the convection cells upwards. If $0 < \theta < \pi$, the enhancement in the lower region and the reduction in the upper region are both displaced leftwards; the effect is that the vertical axis of the convective cell is tilted slightly to the right, with an additional downward ($0 < \theta < \pi/2$) or upward ($\pi/2 < \theta < \pi$) squashing. Conversely, if $-\pi < \theta < 0$, the cells are tilted slightly to the left.

Similar interpretations can be given for other quantities. For example, $|\chi_1|$ and $|\chi_2|$ measure the importance of the first and second harmonics in the concentration perturbation; $\arg(\chi_1)$ describes the horizontal offset between C' and w', while $\arg(\chi_2/\chi_1)$ describes the relative phase of the second harmonic to the first in C', and thus describes the manner in which the concentration perturbations are distorted by the second harmonic. In what follows, we will also consider the porosity perturbation ϕ', defining Φ_1 and Φ_2 in the obvious manner and obtaining them via (3.12).

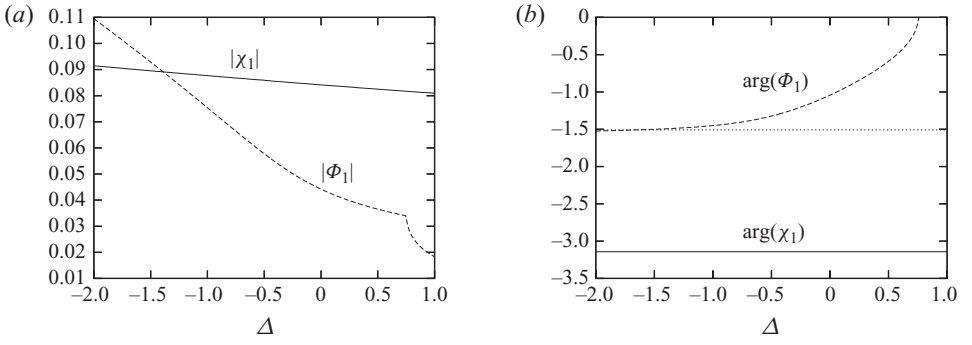

FIGURE 3. (*a*) Amplitudes and (*b*) relative phases of the first harmonics as functions of Δ. In (*a*): solid line, $|\chi_1|$; dashed line, $|\Phi_1|$. In (*b*): solid line, $\arg(\chi_1)$; dashed line, $\arg(\Phi_1)$; dotted line, $-\pi/2$. Parameter values are $\phi_0 = 0.1$, $k_0 = 10$, $\delta = 0.1$ and $m = 3$.

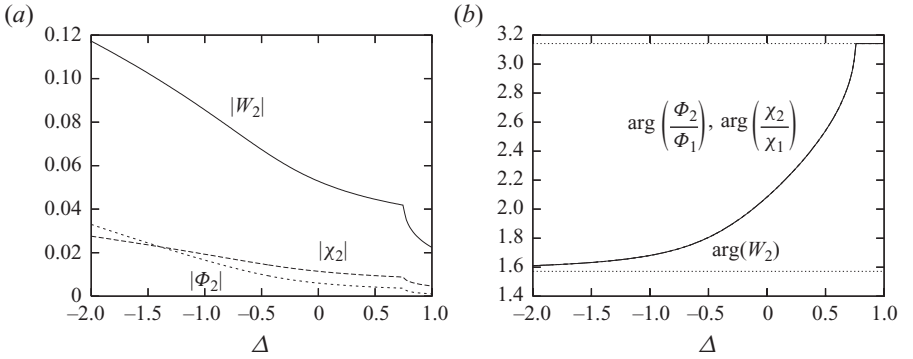

FIGURE 4. (*a*) Amplitudes and (*b*) relative phases of the second harmonics as functions of Δ. In (*a*): solid line, $|W_2|$; heavy dashed line, $|\chi_2|$; light dashed line, $|\Phi_2|$. In (*b*): solid line, $\arg(W_2)$; heavy dashed line, $\arg(\chi_2/\chi_1)$; light dashed line, $\arg(\Phi_2/\Phi_1)$. The three lines are practically indistinguishable. The dotted lines are π and $\pi/2$. Parameter values are $\phi_0 = 0.1$, $k_0 = 10$, $\delta = 0.1$ and $m = 3$.

Figures 3 and 4 show how the amplitudes and phases of the perturbations to vertical velocity, concentration and porosity vary as Δ changes. They should be read in conjunction with figure 5, which illustrates how the corresponding spatial structure of the fastest-growing eigenfunction behaves as Δ is reduced. All the cases plotted in figure 5 lie in the regime where σ is fully complex; the bifurcation point for these parameter values occurs at approximately $\Delta = 0.7$.

For values of Δ to the right of the bifurcation point ($\Delta \approx 0.7$), the perturbations to concentration and porosity are both small (figure 3*a*) and are in phase such that maxima of the first harmonic of ϕ' correspond to minima of the first harmonic of χ (figure 3*b*). A change in trend is immediately noticeable at the bifurcation point: although the first harmonic of concentration continues to vary smoothly, and it remains almost perfectly in phase with the velocity ($\arg(\chi_1) \approx -\pi$, as can be seen in figure 3*b*), the trend in the amplitude of the porosity perturbation alters, and it is no longer perfectly in phase with the concentration perturbation; as $\arg(\Phi_1)$ decreases (figure 3*b*), the extrema of ϕ' move rightwards relative to those of w' and C'.

This is the situation that is beginning to emerge in figures 5(*a*) and 5(*b*), where $\Delta = 0.5$. The pattern of flow, concentration and porosity is very similar to that for

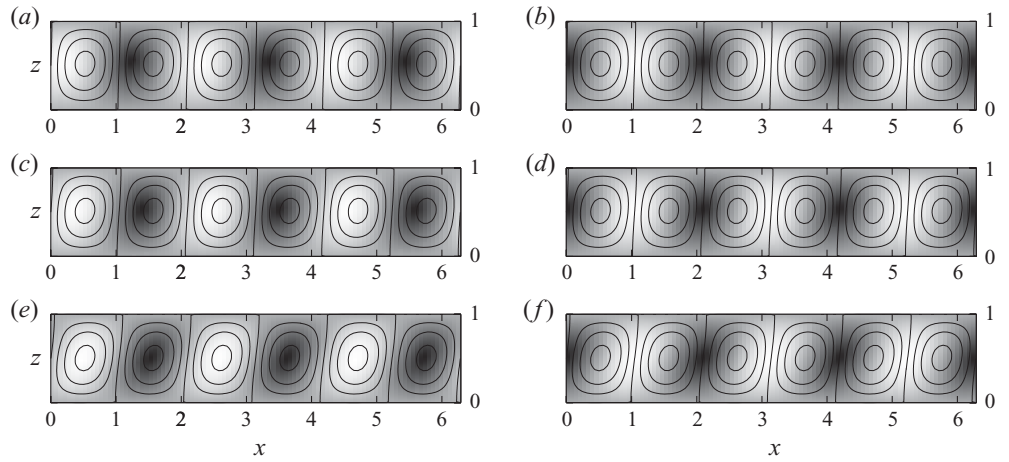

FIGURE 5. Eigenfunctions from the Galerkin analysis, with the leftward-propagating mode taken in each case. (a, c, e) Streamlines superimposed on the ϕ perturbation. (b, d, f) Streamlines superimposed on the C perturbation. Parameters were $\phi_0 = 0.1$, $k_0 = 10$ and $m = 3$. In (a) and (b), $\Delta = 0.5$; in (c) and (d), $\Delta = 0$; in (e) and (f), $\Delta = -1$. In each case, the values of ψ on the streamlines are evenly spaced and in each plot darker shading corresponds to lower values; scales are arbitrary.

simple convection. Downflow draws down higher concentrations from the upper boundary while upflow draws up lower concentrations from the lower boundary. Upflow occurs in high-permeability regions and downflow in low-permeability regions; since the concentration and porosity perturbations are still approximately 'in phase', the reaction will tend to amplify the porosity perturbation. The small phase difference between C' and ϕ' is just apparent, but the distortion caused by the second harmonics is almost imperceptible at this stage.

As Δ is reduced a little further, the concentration and porosity continue to move further out of phase (figure 3*b*), the porosity perturbation grows in importance (figure 3*a*), and the second harmonics start to become apparent. The relative phases of all the second harmonics are in the range $(\pi/2, \pi)$ (figure 4*b*), so they tilt the convection pattern rightwards. This can be seen in figures 5(*c*) and 5(*d*) for $\Delta = 0$; the velocity and concentration perturbations are still closely in phase, but the leftward offset of the porosity perturbation is greater and the rightward tilting of the cells is more evident. Note that it is at roughly this value of Δ that the migration rate of the pattern is greatest (see figure 2*b*).

As Δ is reduced still further, the phase difference between the porosity and concentration perturbations approaches $\pi/2$ (figure 3*b*), so they are almost exactly a quarter of a period out of phase; this is visible in figures 5(*e*) and 5(*f*) ($\Delta = -1$). The importance of the second harmonics increases (figure 4*a*) and their phase difference from the first harmonic approaches $\pi/2$ (figure 4*b*), so they tend to tilt the cells rightwards without squashing them upwards or downwards. The tilting is now clearly evident.

We are now in a position to discuss the mechanisms that maintain this amplifying travelling-wave mode. Recall that the concentration perturbation equation (3.4) contains two source terms which must balance the dissipative effects of the reaction and diffusion terms. The first of these sources is the convective term $-w'$; the second is the term $\partial\phi'/\partial z$, which represents net diffusive transport due to gradients in

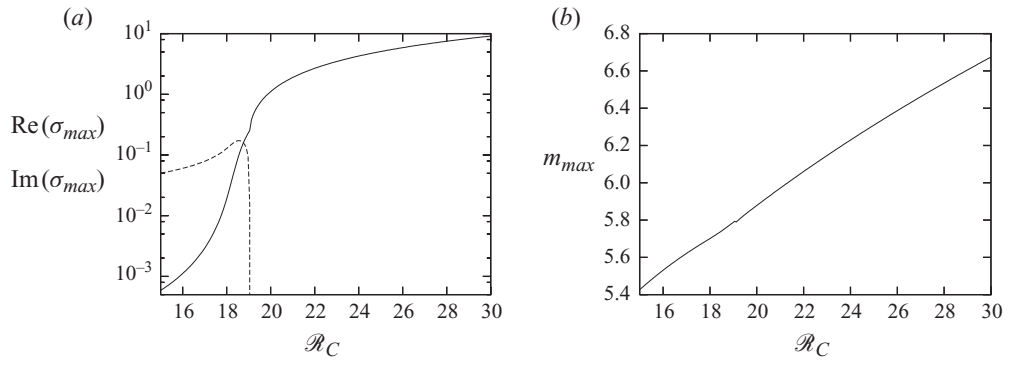

FIGURE 6. (*a*) The real and imaginary parts of the maximum growth rate and (*b*) the corresponding wavenumber. Parameters were $\phi_0 = 0.1$, $k_0 = 10$ and $\delta = 0.1$. In (*a*): solid line, $\mathrm{Re}(\sigma_{max})$; dashed line, $\mathrm{Im}(\sigma_{max})$; note the logarithmic scale.

porosity superimposed on the background vertical gradient of concentration. When the porosity perturbation is weak and the system is dominated by convection, the convective source term dominates. When the porosity perturbation is stronger and convective flow is weak, the importance of the porosity-gradient mechanism increases. Because the porosity perturbation is offset from the concentration perturbation, the effect of this term is felt differently by different parts of the concentration field. Given a 'cell' of high C', it can be seen by comparing figures 5(*e*) and 5(*f*) that the porosity gradient will be negative both to the top left and bottom right of this 'cell', and positive to the top right and bottom left of it. Since the cell is already tilted to the right, this mechanism acts to maintain the tilting against buoyant effects that would tend to restore it to an upright convective cell, and diffusive effects that would tend to eliminate the perturbation altogether. Meanwhile, the offset between C' and ϕ' has the additional effect of causing the porosity perturbations to migrate leftwards. Essentially, then, this mode of behaviour can be characterised as a kind of reaction–diffusion instability which is parasitic on the background vertical concentration gradient.

The modes described here, comprising travelling-wave patterns of tilted cells, are reminiscent of similar patterns seen in mushy layers (Anderson & Worster 1996) and nonlinear simulations of double-diffusive convection (Mamou & Vasseur 1999; Mamou, Vasseur & Hasnaoui 2001). The mechanisms, however, are distinct: the mushy-layer process depends crucially on the release of latent heat and on the time scale of solidification (Anderson & Worster 1996, § 5), while the process in non-reactive convection depends on the double-diffusive effects which permit overdamped oscillations.

3.3.4. *Predictions of stability behaviour*

It is easy to scan systematically across $(\mathscr{R}_C, m)$-space and thus locate the fastest-growing perturbation for each value of $\mathscr{R}_C$; for all values of the parameters considered, there was a single unambiguous maximum over m. We confine the discussion in this section to the branch with the highest value of $\mathrm{Re}(\sigma)$, noting that when $\mathrm{Im}(\sigma) \neq 0$ the complex conjugate of the branch plotted will also be a solution (see figure 2).

Figure 6 illustrates how the wavenumber and growth rate of the fastest-growing perturbation vary with $\mathscr{R}_C$, for a specific value of k_0. In figure 6(*a*), it is clear that the emergence of oscillatory modes at $\mathscr{R}_C \approx 19$ coincides with a rapid, but not

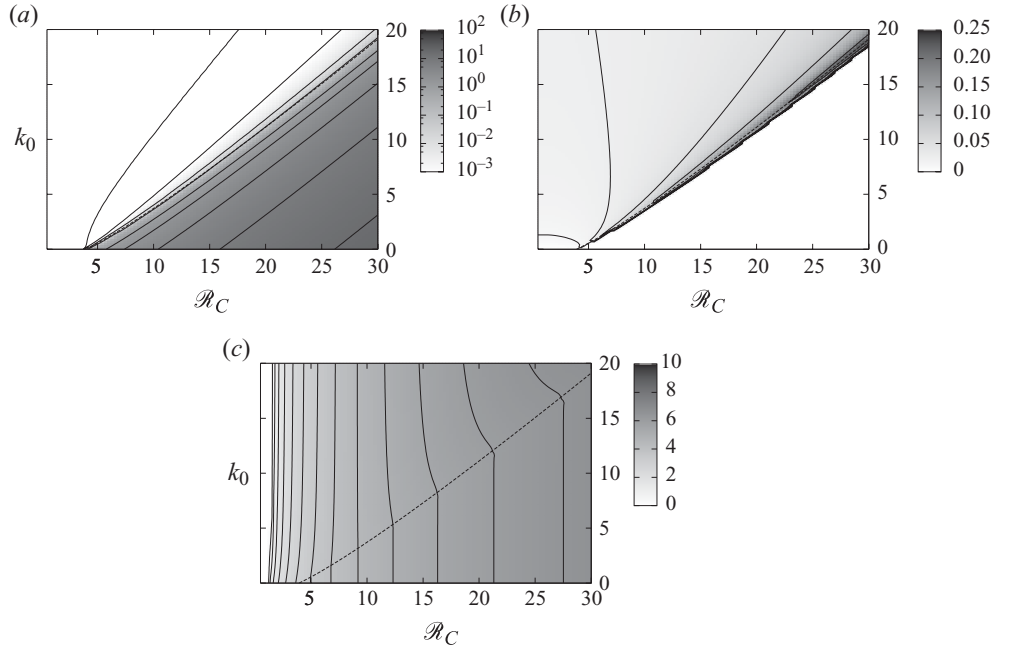

FIGURE 7. Results from the Galerkin analysis with $\phi_0 = 0.1$ and $\delta = 0.1$. (*a*) $\mathrm{Re}(\sigma_{max})$: contours are at $\mathrm{Re}(\sigma_{max}) = 0.0001$, 0.001, 0.01, 0.1, 1, 2, 4, 8 and 16. (Note the logarithmic scale.) (*b*) $\mathrm{Im}(\sigma_{max})$: contours are at $\mathrm{Im}(\sigma) = 0.01$, 0.025, 0.05, 0.1 and 0.2. (*c*) The corresponding wavenumber m_{max}: contours are at intervals of 0.5 starting at $m_{max} = 0.5$. The dashed line in each plot represents $\mathscr{R}_{C,0}^{crit}(k_0)$.

catastrophic, decrease in growth rates. There is a small, but noticeable, rapid change in the favoured wavenumber at this point, which appears to be genuine rather than a plotting artefact.

Figure 7 extends figure 6 to demonstrate how the stability of the system varies with $\mathscr{R}_C$ and k_0, again taking $\delta = 0.1$ to emphasise the effect of the matrix evolution. It is evident from this figure that the stability boundary $\mathscr{R}_{C,0}^{crit}$ from the case $\delta = 0$ provides a good estimate of the boundary between two regimes of behaviour. For $\mathscr{R}_C \gtrsim \mathscr{R}_{C,0}^{crit}$, matrix evolution is insignificant: $\mathrm{Im}(\sigma_{max})$ is zero, and the favoured wavenumber m_{max} increases along the stability boundary but is otherwise independent of k_0 in this regime. For $\mathscr{R}_C \lesssim \mathscr{R}_{C,0}^{crit}$, the travelling-wave mode dominates, with $\mathrm{Re}(\sigma_{max})$ very close to zero and $\mathrm{Im}(\sigma_{max})$ decaying gradually away from the boundary. In this regime, m_{max} does vary somewhat with k_0, and for sufficiently small values of $\mathscr{R}_C$ the favoured wavenumber becomes very small. This indicates that when buoyancy effects are very small, the instability favours extremely long-wave perturbations; in practice, these may not be realised within a finite or a periodic domain.

4. Numerical simulations

A full numerical integration of the system was carried out in order both to test the predictions of the linear stability analysis and to examine the nonlinear behaviour and flow–permeability feedback over longer time scales.

The streamfunction formulation of the system, (B 1)–(B 3), was numerically integrated using the Comsol Multiphysics package. The equations were solved in a rectangular domain, $0 < x < 10$, $0 < z < 1$, and the boundary conditions (B 4) were

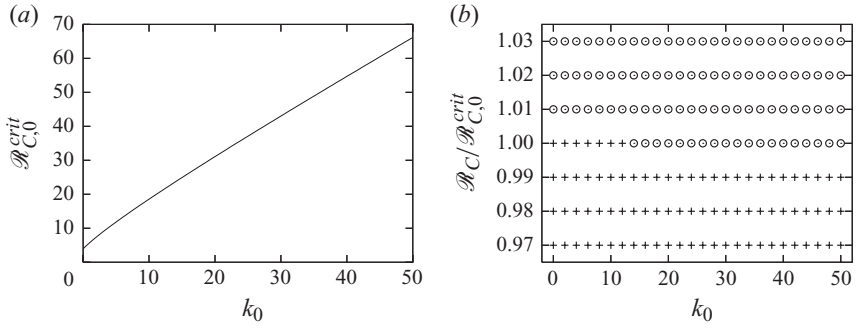

FIGURE 8. (*a*) Stability boundary for $\mathscr{R}_{C,0}^{crit}$ with $\delta = 0$ (3.26). (*b*) $\mathscr{R}_C/\mathscr{R}_{C,0}^{crit}$ from numerical tests with $\phi_0 = 0.1$ and $\delta = 0.001$: the points represent non-convective (+) or convective ($\odot$) behaviour.

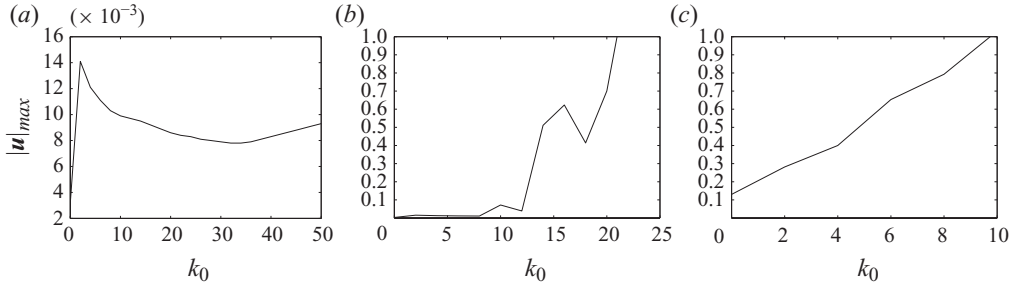

FIGURE 9. Maximum absolute velocity at each reaction rate for (*a*) $\mathscr{R}_C/\mathscr{R}_{C,0}^{crit} = 0.99$, (*b*) $\mathscr{R}_C/\mathscr{R}_{C,0}^{crit} = 1.00$ and (*c*) $\mathscr{R}_C/\mathscr{R}_{C,0}^{crit} = 1.01$.

applied on the horizontal boundaries, while periodicity was imposed on the vertical boundaries. Details of the numerical method are discussed in Appendix B.

4.1. *Stability boundary and the onset of convection*

Figure 8(*a*) shows the critical stability curve when $\delta = 0$ given by (3.26). This curve gives the values of $\mathscr{R}_{C,0}^{crit}$ used in our simulations.

Figure 8(*b*) summarises a large number of numerical experiments carried out to validate the linear stability analysis against the numerics. In each simulation, we took $\phi_0 = 0.1$ and $\delta = 0.001$; each simulation was 1500 time units long and was started from the initial conditions (B 5). This length of simulation ensured that the system had enough time for convection to develop, even in the marginal cases. The criterion used to distinguish between non-convective and convective cases was whether by the end of the simulation the maximum value of $|\boldsymbol{u}|$ was greater or less than 10^{-1}.

Figure 9 shows the maximum absolute velocity for $\mathscr{R}_C/\mathscr{R}_{C,0}^{crit} = 0.99$, 1.00 and 1.01. When $\mathscr{R}_C/\mathscr{R}_{C,0}^{crit} = 0.99$ (figure 9*a*), the maximum velocity was always well below the cutoff point for convective behaviour, and when $\mathscr{R}_C/\mathscr{R}_{C,0}^{crit} = 1.01$ (figure 9*b*) the maximum velocity was always well above the cutoff point. When $\mathscr{R}_C/\mathscr{R}_{C,0}^{crit} = 1.00$ (figure 9*c*), however, we can see the transition from non-convective to convective behaviour at $k_0 \approx 14$.

As can be seen from figure 8(*b*), the linear stability result for $\delta = 0$ (see (3.26)) agrees well with the numerical results. This suggests, in agreement with § 3.3, that the effects of porosity evolution on the onset of convection are rather subtle.

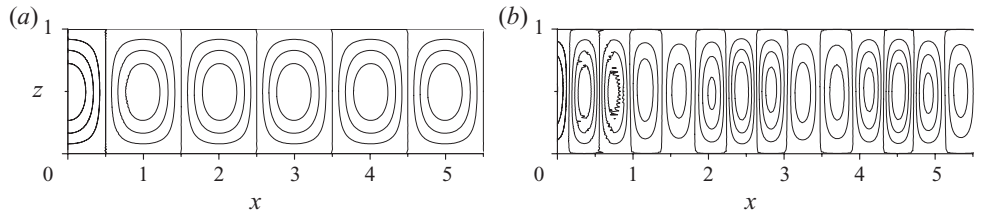

FIGURE 10. Streamlines for simulations with (*a*) $k_0 = 0$ and (*b*) $k_0 = 40$. In both cases, there was no porosity evolution ($\delta = 0$) and the Rayleigh number was 1 % above the critical Rayleigh number given by (3.26). The irregularities in the streamlines around $x = 0.75$ are artefacts of the plotting software, caused by the irregular mesh triangulation in this region.

A key qualitative prediction of the linear stability analysis is that along the line $\mathscr{R}_C = \mathscr{R}_{C,0}^{crit}$, the wavelength of the fastest-growing perturbations should increase with the reaction rate. Figure 10 shows the streamlines for two simulations: one with no reaction ($k_0 = 0$) and one with a higher reaction rate ($k_0 = 40$). In each case, the Rayleigh number was 1 % above the critical Rayleigh number given by (3.26). For no reaction, both (3.25) and the numerics give a wavenumber of π. For $k_0 = 40$, (3.25) predicts the wavenumber to be $m_0^{crit} \approx 7.98$, and the numerical results show the wavenumber to be $m \approx 7.54$. The discrepancy can be attributed to the horizontal periodicity of the numerical domain; the numerical value of m corresponds to 12 pairs of counter-rotating cells in $0 \leqslant x \leqslant 10$, while the theoretically predicted value would require between 12 and 13 such pairs. Similar discretisation errors were noted by Pritchard & Richardson (2007).

4.2. *Long-term behaviour*

When examining the long-term behaviour of the system, we will pay particular attention to two cases: one with a slower reaction $k_0 = 10$ and one with a faster reaction $k_0 = 30$. Each simulation we describe lasted for 5000 time units and employed the parameters $\phi_0 = 0.1$ and $\delta = 0.001$. We will present results for four values of the Rayleigh number: the critical Rayleigh number given by (3.26), and 10 %, 20 % and 50 % above this value.

4.2.1. *Reference case:* $k_0 = 10$ *and* $\mathscr{R}_C = 1.1\mathscr{R}_{C,0}^{crit}$

We first consider the slow reaction with $k_0 = 10$. As a reference case for the long-term behaviour, we begin by focusing on the simulation with a Rayleigh number 10 % above the critical value, $\mathscr{R}_C = 20.42$ (compared with $\mathscr{R}_{C,0}^{crit} \approx 18.56$). Figure 11 shows the evolution of the concentration perturbation C', the porosity ϕ and the absolute velocity $|\boldsymbol{u}|$ for the left half of the domain. The solid lines on the concentration and porosity plots are the streamlines and the arrows on the absolute velocity plot indicate the velocity field.

By $t = 100$, steady convection has been established (figure 11*a*). At this time, the concentration and porosity fields are in phase; that is, regions of $C' > 0$ coincide with regions of lower porosity ($\phi < \phi_0$) and regions of $C' < 0$ coincide with regions of higher porosity ($\phi > \phi_0$). From (3.5), we expect porosity to decrease where $C' > 0$ and to increase where $C' < 0$. As the flow is buoyancy-driven, downward flow is favoured where $C' > 0$, drawing down higher concentrations from the top boundary, and upward flow is favoured where $C' < 0$, drawing up lower concentrations from the bottom boundary: this is the essential mechanism that sustains convection. Furthermore, flow is faster in areas of higher porosity, shown by the closer packed streamlines in

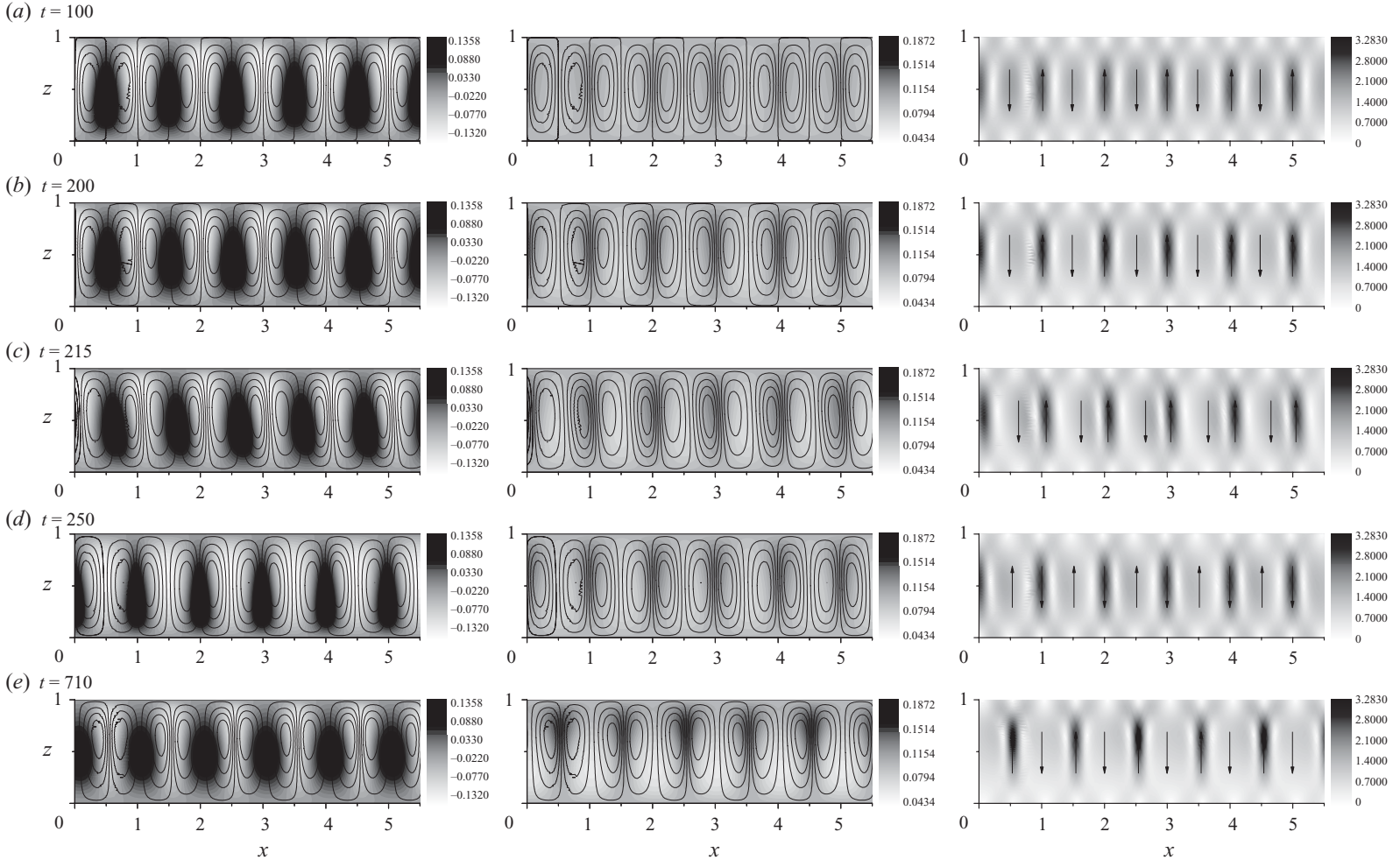

FIGURE 11. See caption on next page.

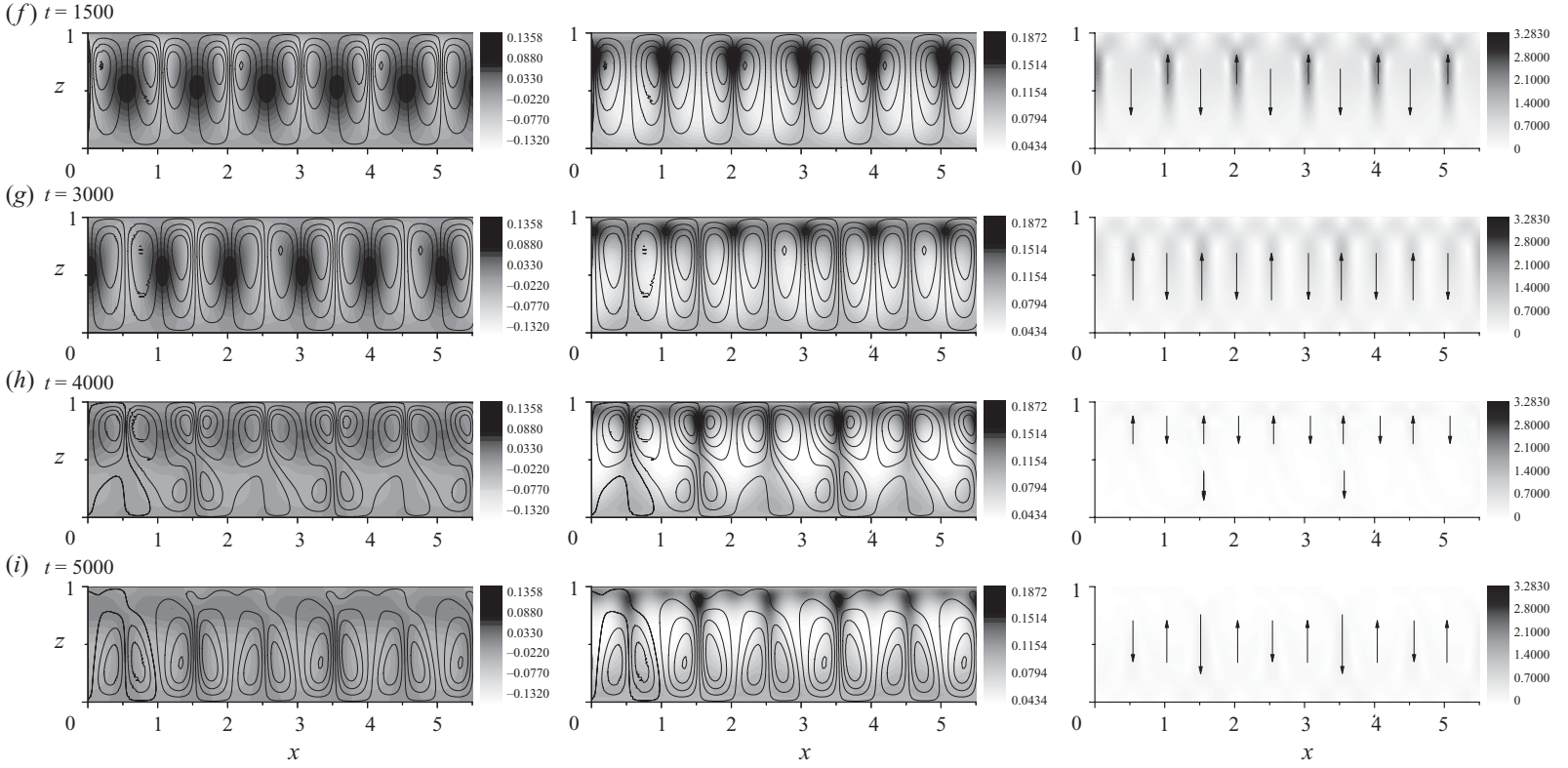

FIGURE 11. (*a–i*) Evolution with $k_0 = 10$. Shading indicates solutal concentration perturbation C' (left), porosity ϕ (centre) and absolute velocity $|\boldsymbol{u}|$ (right). Solid lines are streamlines and arrows indicate the velocity field but are not drawn to scale. The irregularities in the streamlines around $x = 0.75$ are artefacts of the plotting software, caused by the irregular mesh triangulation in this region.

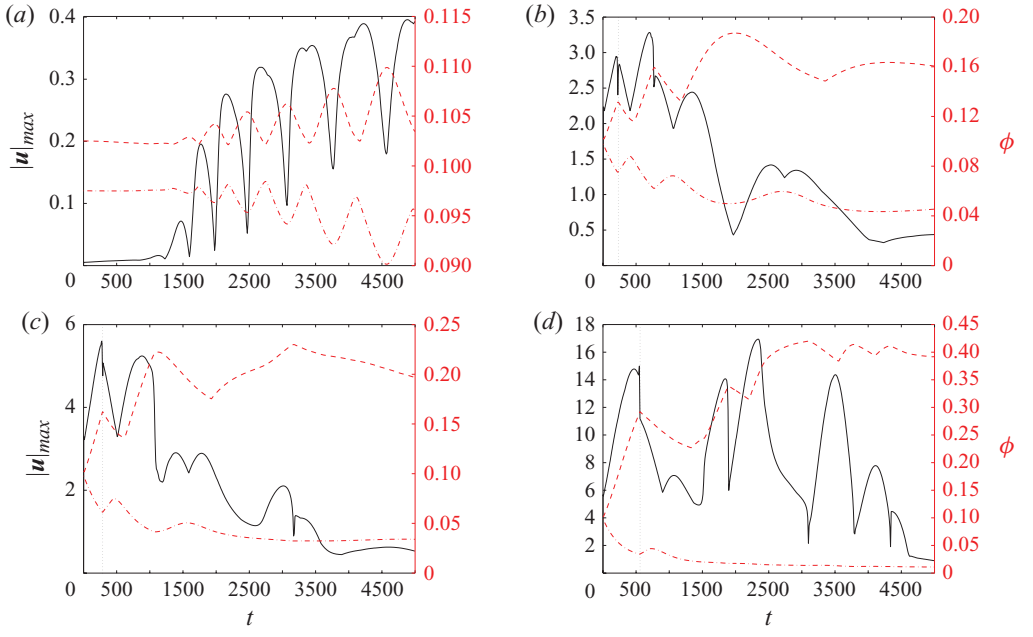

FIGURE 12. (Colour online) Maximum absolute velocity $|\boldsymbol{u}|$ and maximum and minimum porosity ϕ throughout the whole domain when $k_0 = 10$. Solid line, maximum velocity; dashed line, maximum porosity; dash-dotted line, minimum porosity. In (*a*) $\mathscr{R}_C = \mathscr{R}_{C,0}^{crit}$, (*b*) $\mathscr{R}_C = 1.1\mathscr{R}_{C,0}^{crit}$, (*c*) $\mathscr{R}_C = 1.2\mathscr{R}_{C,0}^{crit}$ and (*d*) $\mathscr{R}_C = 1.5\mathscr{R}_{C,0}^{crit}$.

regions of $\phi > \phi_0$ which coincide with the darker areas of the absolute velocity field. Therefore, as can be seen from the arrows on the absolute velocity plot, upward flow is faster than downward flow.

Once steady convection has been established, the porosity field continues to evolve until it triggers a secondary instability in the form of a phase shift. Figure 11(*b*) shows the fields at $t = 200$, just before the phase shift. Comparing with figure 11(*a*), we can see that although the concentration field is the same, the porosity field has evolved further and now has more pronounced areas of high and low porosity. As a result of this evolution, the absolute velocity field now has more pronounced areas of upward flow coinciding with areas of higher porosity. The centres of the circulation cells have also moved upwards slightly.

Part-way through the shift ($t = 215$, figure 11*c*), the concentration field has moved approximately an eighth of a cell (0.25 x-units) to the right, but the porosity field remains the same as before the shift. Also, in the absolute velocity field we see that the upward flow has remained in approximately the same position, but the downward flow has shifted towards the right, while there is a slight tilting of the cells to the left (most apparent in the concentration field). By the end of the shift at $t = 250$ (figure 11*d*), the concentration field and streamlines have moved a half cell (one x-unit) to the right, and the centre of the circulation cells has moved slightly downward, but the porosity field is still effectively unchanged. There is still downward flow where $C' > 0$, but this now coincides with high-porosity regions. Therefore, downward flow is now faster than upward flow.

Further evidence of this phase shift can be seen in figure 12(*b*), which shows the maximum absolute velocity throughout the whole domain. From these figures, we

see that convection develops and is maintained for approximately 200 time steps, but there is a dip in the velocity around the time of the phase shift as the circulation slows and then re-establishes itself. After this shift, the system settles back into a quasi-equilibrium state of almost steady convection.

The secondary instability occurs as a result of the positive feedback between the concentration and porosity fields which causes clogging in the downflow regions. This clogging eventually reaches some critical state and displaces the downflow sideways, resulting in narrower, tilted convection cells. These are overcome by diffusion and the circulation begins to shut down before it is replaced by a reversed circulation. Bolton *et al.* (1999) identified a similar mechanism which acted to displace the 'stalk' of rising thermal plumes in their simulations. The sideways migration of these fully developed, nonlinear convection cells is also reminiscent of the migration of small-amplitude cells seen in the linear analysis close to $\mathscr{R}_C = \mathscr{R}_{C,0}^{crit}$ (§ 3.3.3). Unlike the phenomenon seen in the linear case, the tilting and sideways movement here is readily halted by the tendency of buoyancy-driven convection to favour stationary, upright cells.

At $t = 250$ (figure 11*d*), the concentration and porosity fields are out of phase: areas of large positive concentration perturbations now coincide with areas of high porosity and vice versa. In these high concentration ($C' > 0$) areas porosity will decrease, and in low concentration ($C' < 0$) areas porosity will increase. Therefore, the porosity evolution strives to get the concentration and porosity fields back into phase.

The porosity evolution is shown in figure 12(*b*), plotted with the maximum absolute velocity to display the correlation with the phase shifts. At the time of the phase shift (denoted by the vertical dotted line), the porosity contrast has reached a local maximum, with a peak in the maximum porosity and a trough in the minimum porosity. After the shift, the maximum porosity decreases and the minimum porosity increases, because the concentration and porosity fields are now out of phase. By $t \approx 500$, the concentration and porosity fields are back in phase and so now the porosity contrast begins to increase again at a rate similar to that before the phase shift.

By $t = 710$ (figure 11*e*), the porosity is back in phase with the concentration field. There is faster upward flow in regions of higher porosity and slower downflow in low porosity regions, as before the first phase shift. Note that there is now a distinct vertical asymmetry in the circulation and porosity field: there is more dissolution towards the top of the domain and the circulation has correspondingly moved upwards to this higher porosity region. After this, the system goes through another phase shift, again moving one half cell to the right, displaying the same behaviour as with the first shift. This shift can be seen in figure 12(*b*) as the sharp dip in $|\boldsymbol{u}|_{max}$ at $t \approx 750$. These figures also show porosity behaviour similar to that during the first phase shift, with the porosity contrast peaking around the time of the shift.

From figure 12(*b*) we can see that the system only undergoes two rapid phase shifts, and subsequent changes take place over a much longer time scale. By $t = 1500$ (figure 11*f*), the system is back in phase, but with the circulation field shifted a further quarter cell to the right. There is now a more distinct vertical asymmetry in the circulation and porosity fields, with higher porosity regions and the centres of the circulation cells now even closer to the top of the domain. Also, the magnitude of the concentration perturbations and the absolute velocity are reduced.

By $t = 3000$ (figure 11*g*), the circulation has shifted a further quarter cell to the right but the system is still in phase, with upflow concentrated in more highly permeable vertical channels. Alternate high-permeability channels are more pronounced; this can be explained as the result of an instability whereby a slightly more permeable

channel 'steals' flux from its neighbours and thus experiences more rapid dissolution. This is akin to the 'screening' effect that causes dissolution patterns to be dominated by a few large fingers (Daccord 1987; Hoefner & Fogler 1988). This screening effect competes with the convective circulation to set the favoured wavenumber of the system, leading to the alternation that is observed. There is a superficial similarity between the high-permeability channels here and the chimneys observed in mushy layers (Worster 1997), although the channels here are merely regions of enhanced porosity rather than regions where the porous matrix has been entirely dissolved. The layering of high porosity over lower porosity regions is also more pronounced at this stage than at earlier times.

The slow evolution continues and by $t = 4000$ (figure 11*h*) the fields have changed considerably. The concentration perturbations are now very small and there is distinct layering in the porosity field, with a low porosity barrier in the middle of the domain which is pierced by occasional high-porosity channels. This barrier cannot extend to the lower boundary since the boundary conditions there fix the concentration at its equilibrium value C_{eq}, and hence fix the porosity at $\phi = \phi_0$. There is still evidence of the period-doubling seen at earlier times, with alternate high-porosity channels more pronounced. From the streamlines and the absolute velocity field, we see that because of this barrier, two-layered convection has developed. In the top layer, the concentration and porosity fields are in phase, but in the bottom layer they are out of phase.

By the end of the simulation at $t = 5000$ (figure 11*i*), only the lower layer where the concentration and porosity fields are out of phase has survived and it now penetrates the upper layer. The period-doubling has survived, but there is now more pronounced downflow in alternate high-porosity channels. Note that even after more than 1000 time units, the lower layer has not yet reversed phase.

4.2.2. *Effect of varying the Rayleigh number*

Figure 12 shows the porosity evolution and maximum absolute velocity for each of the convective Rayleigh numbers with $k_0 = 10$. Initial adjustment to steady convection happens very rapidly, within roughly the first 10 time units. The system then evolves gradually until the first phase shift, the signature of which is a sharp drop in the maximum absolute velocity. The higher the Rayleigh number, the longer it is before the phase shift occurs. The porosity contrast is at its greatest when a phase shift occurs, and the higher the Rayleigh number, the greater the porosity change when the system shifts. This behaviour is expected since as we increase the Rayleigh number, we are increasing the concentration difference between the top and bottom of the domain. Therefore, we expect to see bigger absolute velocities and require bigger porosity differences to trigger a phase shift.

When $\mathscr{R}_C = \mathscr{R}_{C,0}^{crit}$, the system appears for around 1000 time steps to be non-convective (figure 8*b*), but after this time a weak circulation does develop (figure 12*a*). This reflects the fact that even at or below the 'threshold' $\mathscr{R}_C = \mathscr{R}_{C,0}^{crit}$, the system remains weakly unstable, as shown in § 3.3. Meanwhile, when $\mathscr{R}_C = 1.2\mathscr{R}_{C,0}^{crit}$ and $\mathscr{R}_C = 1.5\mathscr{R}_{C,0}^{crit}$, we see behaviour similar to that with $\mathscr{R}_C = 1.1\mathscr{R}_{C,0}^{crit}$, although with more rapid and vigorous evolution.

4.2.3. *Effect of varying the reaction rate*

We now consider the faster reaction with $k_0 = 30$. To allow a direct comparison with the long-term behaviour in the slow reaction case, we focus on a simulation with a Rayleigh number 10 % above the critical value, $\mathscr{R}_C = 47.34$ compared with

$\mathscr{R}_{C,0}^{crit} \approx 43.03$. Figure 13 shows the evolution of the concentration perturbation C', the porosity ϕ and the absolute velocity $|\boldsymbol{u}|$ for the left half of the domain, while figure 14 shows the corresponding evolution of the maximum velocity and the porosity contrast. The most prominent difference between figure 14 and figure 12 is that the higher reaction rate and higher Rayleigh number lead to faster evolution of the system. What is of more interest is whether the qualitative development also changes.

Buoyancy-driven convection has been established by $t \approx 10$ (not shown); at this time, the convection pattern closely resembles figure 11(*a*), and there are 10 pairs of counter-rotating cells in the full domain, corresponding to a wavenumber of $m \approx 6.28$, compared with the critical wavenumber $m_0^{crit} \approx 7.44$ predicted by (3.25). By $t = 50$ (figure 13*a*), additional convection cells have appeared at $x \approx 3.5$ and $x \approx 9.5$. These subsequently expand so that there are 12 pairs of counter-rotating cells in the domain, corresponding to a wavenumber of $m \approx 7.54$. The emergence of the two pairs of counter-rotating cells, on top of an existing although weakly defined porosity structure, results in a less uniform cell pattern, with some cells now tilting and slightly more pronounced upflow in some channels than others (figure 13*b*). Note from figure 14 that the emergence of the extra cells does not affect the maximum absolute velocity.

Once convection has been established with an appropriate wavenumber, the porosity field evolves until it triggers a secondary instability, as with the slower reaction rate (§ 4.2.1). Figure 13(*b*) shows the fields at $t = 180$, just before the phase shift (compare figure 11*b* for the case $k_0 = 10$). As before, the concentration perturbation and porosity fields are initially in phase before the shift, while after the phase shift ($t = 210$, figure 13*c*) the concentration perturbation field and streamlines have moved a half cell (≈ 1 x-unit) to the right, and now the cells are more upright. Furthermore, the concentration perturbation and porosity fields are now out of phase. The overall pattern is similar to figure 11(*d*), although the strengths of the cells are less uniform; this may be because the faster reaction promotes the 'screening' effect in which cells compete with their neighbours for flux (§ 4.2.1).

The phase shift can also be seen in the maximum absolute velocity and porosity contrast (figure 14). Convection develops and is maintained for almost 200 time steps, but there is a dip in the velocity around the time of the phase shift (marked by the vertical dotted line) as the circulation slows and then re-establishes itself. After this shift, the system settles back into a quasi-equilibrium state of steady convection, with the maximum velocity and porosity contrast first declining and then gradually increasing again as the porosity comes back into phase with the concentration. (Precisely analogous behaviour can be seen in figure 12.)

By $t = 380$ (figure 13*d*), the concentration and porosity fields are back in phase, although the porosity perturbations are small and the centres of the circulation cells have moved upwards. No further rapid phase shifts occur, but the slow evolution continues. At first, the porosity contrast becomes more pronounced, with 'eyes' of high porosity developing at the top of the layer and regions of lower porosity in the middle of the domain; meanwhile, the circulation pattern becomes more irregular than § 4.2.1, with a weak lower layer of counter-rotating cells forming in places and flow in the middle of the layer focussed into a few narrow channels (figure 13*e*); the picture is reminiscent of figure 11(*h*), but the flow pattern is more irregular and the overall porosity contrast more strongly dominated by the 'eyes' near the upper boundary. As the simulation continues, the qualitative picture is unaltered (figure 13*f*), but the porosity and the maximum velocity both gradually decline (figure 14). This

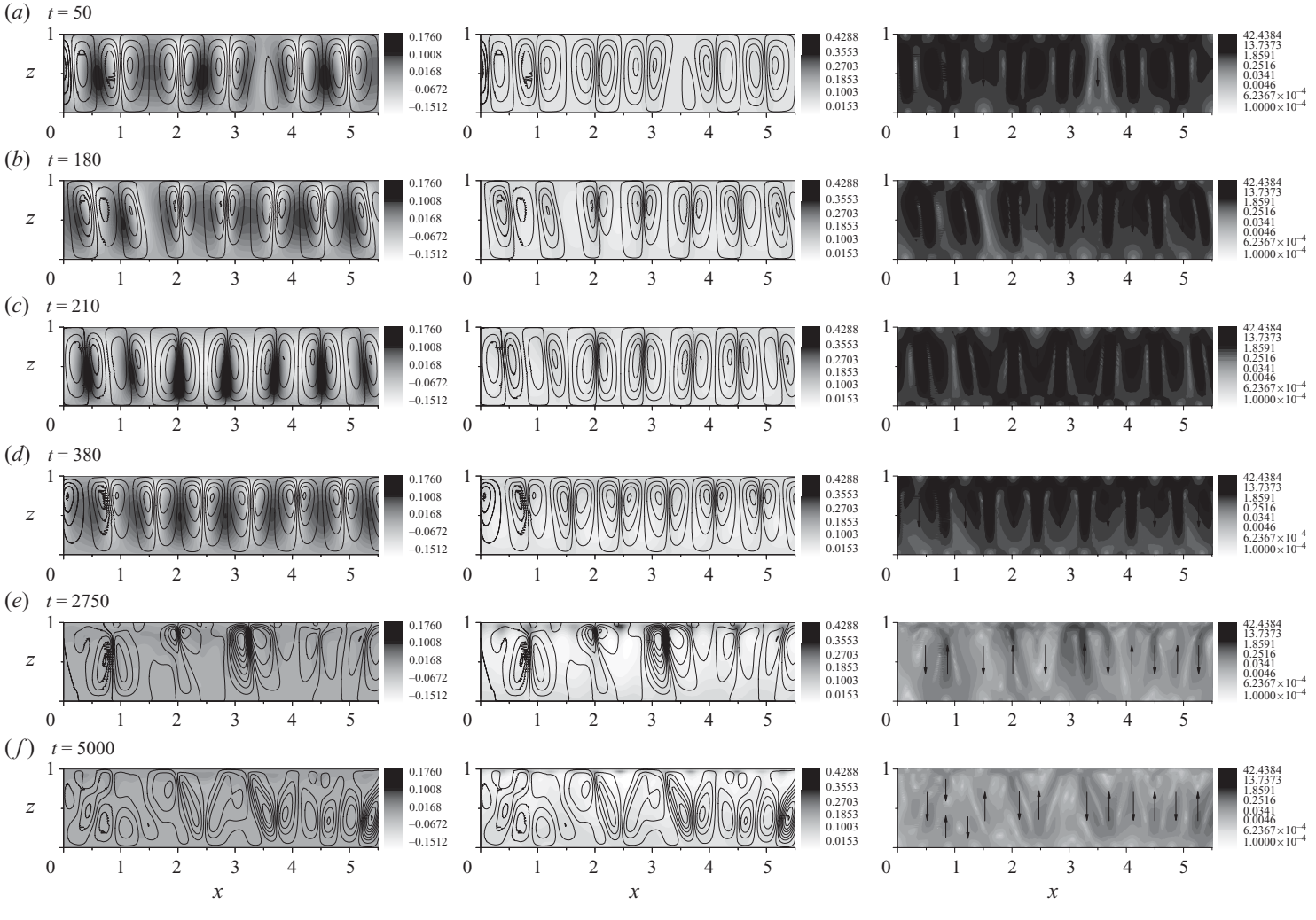

FIGURE 13. (*a–f*) Evolution with $k_0 = 30$. Shading indicates solutal concentration perturbation C' (left), porosity ϕ (centre) and absolute velocity $|\boldsymbol{u}|$ (right). Solid lines are streamlines and arrows indicate the velocity field but are not drawn to scale. The irregularities in the streamlines around $x = 0.75$ are artefacts of the plotting software, caused by the irregular mesh triangulation in this region.

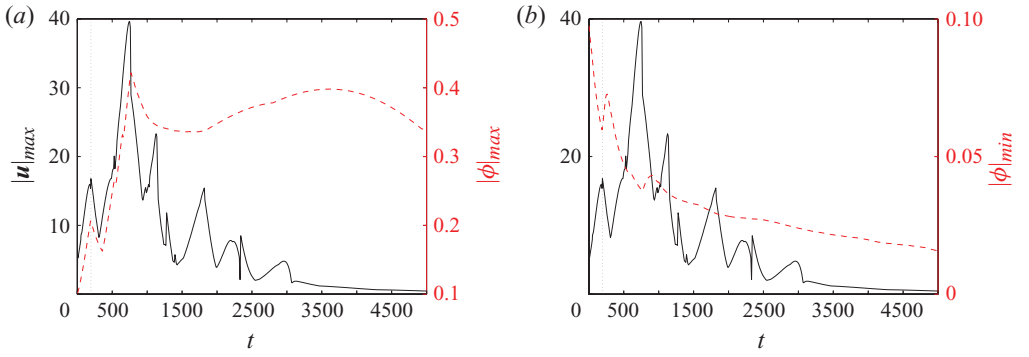

FIGURE 14. (Colour online) Maximum absolute velocity $|\boldsymbol{u}|$ and (a) maximum and (b) minimum porosity ϕ throughout the whole domain when $\phi_0 = 0.1$, $\delta = 0.001$, $k_0 = 30$ and $\mathscr{R}_C = 1.1\mathscr{R}_{C,0}^{crit}$. Solid line, the maximum velocity; dashed line, the maximum or minimum porosity.

suggests that the very long-term attractor of the system may be a non-convective state with a considerably decreased porosity throughout the layer.

4.2.4. *Summary of long-term behaviour*

A common feature of all the numerical experiments is the interaction between processes operating at different time scales. There is always a rapid hydrodynamic adjustment, over dimensionless time scales of the order of 1–10, which seeks to establish a steady convective circulation pattern modulated by the instantaneous porosity structure. Over a slower time scale, of the order of 100 in our experiments, there is a tendency for cells to 'brand' themselves on the matrix by establishing and reinforcing an in-phase porosity pattern. This reinforcement, though, must compete with the secondary instability, associated with the clogging and displacement of high-concentration downflows, which drives occasional phase shifts that reverse the direction of the circulation over time scales of the order of 10 in our experiments. Over extremely long time scales (of the order of 1000 in our experiments), the repeated interaction between these different processes tends to lead to layered porosity structures penetrated by narrow vertical channels; there is some suggestion that ultimately the system may tend towards a non-convective state in which the porosity is everywhere higher than its initial value.

Higher Rayleigh numbers generally lead to more rapidly established and more strongly maintained convective circulation; the onset of secondary instabilities is delayed but not prevented by higher values of $\mathscr{R}_C$. Similarly, higher reaction rates favour more rapid evolution of the system and bring forward the occurrence of the secondary instability. They also accelerate the very slow evolution, potentially reducing the time until the convection can modify the rock enough to efface itself altogether.

5. Summary and conclusions

We have investigated the behaviour of an idealised mathematical model of geochemical convection in a reactive porous medium. The model can be obtained from the thermosolutal model of Pritchard & Richardson (2007) in the limit of very high thermal diffusivity and finite solutal diffusivity with negligible thermal expansion, but it also incorporates the novel feature of evolving porosity and permeability fields.

Although the porosity evolution is slow on the time scale of convection and reaction, it exerts an unexpected influence on the stability properties of the system. When

the system is strongly buoyantly unstable, the reaction acts to remove destabilising solute and thus to stabilise the system. However, when the system is close to the threshold of instability (as calculated without porosity evolution), a new unstable mode becomes available and persists even when the Rayleigh number is reduced below the critical value for buoyant instability. This new mode is essentially a reaction–diffusion instability which is driven by solute fluxes caused by the interaction between the porosity perturbation and the background vertical concentration gradient.

Over longer time scales, the porosity evolution introduces further new behaviour; although quasi-steady convective circulation becomes established as in non-reactive convection, it cannot persist indefinitely. Instead, the porosity changes associated with the circulation become steadily more pronounced, and ultimately trigger a relatively rapid reorganisation of the flow in which the entire pattern of convective cells shifts sideways by half a wavelength.

The repeated interplay between episodes of quasi-steady convection and the rapid reorganisations that punctuate them eventually develops a layered porosity structure, with the centre of the layer being dominated by a low-porosity band broken by occasional higher-permeability vertical channels and pockets of enhanced porosity occurring nearer the top and bottom of the layer. There appears to be no long-term steady convective state towards which the system asymptotes, although once layering has become established there is a tendency for the strength of convection to decrease.

These findings complement the numerical experiments of Bolton *et al.* (1996, 1997, 1999) by demonstrating that geochemical convection can spontaneously give rise to heterogeneous porosity fields, and not merely enhance heterogeneities that already exist. Their wider implication is that in situations in which long-term convective transport is simulated in order to determine patterns of mineralisation, such as ore deposition (e.g. Raffensperger & Garven 1995*a*,*b*), it may be essential to incorporate flow–reaction–permeability coupling in order to capture even the outline of the mineralisation patterns. Another implication is that because of the development of instabilities which scale in a nonlinear manner with the matrix evolution rate δ, simulations which accelerate the rock evolution to reduce runtime may thereby distort their results in unexpected ways. This implication was supported by further numerical simulations (omitted here for brevity) which found that increasing δ by a factor of 10 resulted in more pronounced tilting of the circulation cells, as well as triggering earlier and more frequent episodes of rapid flow reorganisation and a more strongly layered porosity structure.

The most natural extension of the work described here is to the full thermosolutal system. Work on this problem is ongoing, and may be expected to yield further intricate connections between flow, reaction and rock evolution processes. More detailed models of the geochemistry, including multiple species or more complicated reaction laws, could also readily be considered; the hope is that the fundamental interactions described here will provide a basis for understanding such systems.

In summary, investigating this apparently minor extension to the classic problem of convection in a porous medium has revealed surprisingly rich dynamical behaviour, and hints that the geological signature of convective processes may not be immediately recognisable as such. After more than 60 years of mathematical investigation, it appears that geochemical convection has lost none of its fascination or its ability to surprise.

L.T.R. is supported by a scholarship from the Carnegie Trust for the Universities of Scotland. We are grateful to Professor Nigel Mottram for assisting us to set up the

problem in Comsol. We would also like to thank three anonymous referees for their suggestions for improvement of the original manuscript.

Appendix A. Technical details of various mathematical results

A.1. *Principle of the exchange of stabilities when* $\delta = 0$

Adapting the approach of Chandrasekhar (1961, § 11), we show that for the reduced problem with a reaction but no matrix evolution, the principle of the exchange of stabilities is valid, so marginal stability is characterised by $\sigma = 0$. Throughout this appendix, we will use the notation $D = \mathrm{d}/\mathrm{d}z$ for brevity.

Let $G(z) = (D^2 - m^2)W(z)$, so (3.13), with $\delta = 0$, becomes

$$[\phi_0(D^2 - m^2) - (k_0 + \sigma)]G(z) = m^2 \mathscr{R}_C W(z), \tag{A 1}$$

where $W(z)$ and $G(z)$ must satisfy the boundary conditions

$$W(z) = 0 \quad \text{and} \quad G(z) = 0 \quad \text{at} \quad z = 0 \quad \text{and} \quad z = 1. \tag{A 2}$$

We multiply (A 1) by G^*, the complex conjugate of G, and integrate over the range of z, obtaining

$$\int_0^1 G^*[\phi_0(D^2 - m^2) - (k_0 + \sigma)]G \,\mathrm{d}z = m^2 \mathscr{R}_C \int_0^1 G^* W \,\mathrm{d}z. \tag{A 3}$$

Integrating by parts and using $G(z) = (D^2 - m^2)W(z)$, this may be rewritten as

$$\int_0^1 \{\phi_0 |DG|^2 + (\phi_0 m^2 + k_0 + \sigma)|G|^2\} \,\mathrm{d}z - m^2 \mathscr{R}_C \int_0^1 \{|DW|^2 + m^2 |W|^2\} \,\mathrm{d}z = 0. \tag{A 4}$$

The real and imaginary parts of (A 4) must vanish separately. The imaginary part is given by

$$\mathrm{Im}(\sigma) \int_0^1 |G|^2 \,\mathrm{d}z = 0, \tag{A 5}$$

which is satisfied only if $\mathrm{Im}(\sigma) = 0$. Therefore, σ must be real, and marginal stability is characterised by $\sigma = 0$.

A.2. *Asymptotic analysis of the quartic in the Galerkin approach*

To analyse the asymptotic behaviour of σ, it is helpful to rewrite the quartic (3.38) as

$$a_4\sigma^4 + (b_3 - c_3\Delta)\sigma^3 + (d_2\Delta^2 - c_2\Delta)\sigma^2 + b_0\delta^2 = 0, \tag{A 6}$$

where all the constants a_i, b_i, c_i and d_i are positive and of order unity; they can readily be extracted from (3.39)–(3.43). We will always take $\delta \ll 1$ and seek asymptotic scalings for σ and Δ in terms of δ.

A.2.1. *Small* Δ*: location of the bifurcation point*

We start by looking at the asymptotics for $\Delta \ll 1$. We first eliminate all terms in (A 6) which must be sub-dominant, obtaining

$$a_4\sigma^4 + b_3\sigma^3 - c_2\Delta\sigma^2 + b_0\delta^2 \approx 0. \tag{A 7}$$

There will always be a negative, order-unity solution $\sigma \sim -b_3/a_4$; all other roots of the quartic must be small in magnitude. Taking $\sigma \ll 1$ and retaining only possible dominant terms, we can reduce the equation further to the cubic

$$b_3\sigma^3 - c_2\Delta\sigma^2 + b_0\delta^2 \approx 0. \tag{A 8}$$

The bifurcation can occur if all three of these terms are of the same order. This requires $\sigma \sim \delta^{2/3}$ and $\Delta \sim \delta^{2/3}$, so we set $\sigma = \delta^{2/3}\Sigma$ and $\Delta = \delta^{2/3}D$, with Σ and D of order unity, to obtain

$$f(\Sigma) \equiv b_3\Sigma^3 - c_2 D\Sigma^2 + b_0 \approx 0. \tag{A 9}$$

It is apparent by inspection that for sufficiently large D, (A 9) will have three real roots, while for smaller values of D there will be only one real root and two complex ones. We locate the bifurcation point by requiring $f(\Sigma) = 0$ and $f'(\Sigma) = 0$ simultaneously, yielding

$$b_3\Sigma^3 - c_2 D\Sigma^2 + b_0 = 0 \quad \text{and} \quad 3b_3\Sigma^2 - 2c_2 D\Sigma = 0. \tag{A 10}$$

As $\Sigma = 0$ is not an admissible possibility, the bifurcation must occur when

$$\Sigma = \frac{2c_2 D}{3b_3} \quad \text{and thus} \quad b_3\left(\frac{2c_2 D}{3b_3}\right)^3 - c_2 D\left(\frac{2c_2 D}{3b_3}\right)^2 + b_0 = 0, \tag{A 11}$$

finally yielding

$$-\frac{4c_2^3 D^3}{27b_3^2} + b_0 = 0 \iff D = \left(\frac{27b_3^2 b_0}{4c_2^3}\right)^{1/3}, \quad \text{and hence} \quad \Sigma = \left(\frac{2b_0}{b_3}\right)^{1/3}. \tag{A 12}$$

Comparisons (not shown) of (A 12) with numerical solutions of (3.38) suggest that these asymptotics capture the behaviour of the solutions well.

A.2.2. *Regular perturbation to* σ_0

When $\Delta = \mathcal{O}(1)$, we expect that there will be a solution branch with $\sigma \approx \sigma_0$. To locate this branch, we set $\sigma = \sigma_0 + \sigma_1$ in (A 6), obtaining an equation of the form

$$A_4\sigma_1^4 + A_3\sigma_1^3 + A_2\sigma_1^2 + A_1\sigma_1 + B_0\delta^2 = 0, \tag{A 13}$$

where all constants except δ and σ_1 are implicitly of the order of 1, though not necessarily positive. Seeking a regular perturbation so $\sigma_1 \ll 1$, this reduces to

$$A_1\sigma_1 + B_0\delta^2 \approx 0, \quad \text{i.e.} \quad \sigma_1 \sim -\frac{B_0}{A_1}\delta^2. \tag{A 14}$$

Thus, the effect of matrix evolution on the growth rate of instabilities is negligibly small, $\mathcal{O}(\delta^2)$, as long as we are away from the $\delta = 0$ stability boundary.

A.2.3. *Behaviour as* $\Delta \to -\infty$

Finally, we investigate the behaviour of the dominant solution branch as $\Delta \to -\infty$. Taking $\sigma \sim \Delta^\alpha$ for some α, we find two possibilities. If $\alpha = 1$ then we have a balance between the σ^4, σ^3 and σ^2 terms, and it is easy to show that both resulting solutions have negative real part. More interestingly, for any negative value of α we find that the balance must be between the σ^2 and σ^0 terms, eventually giving solutions of the form

$$\sigma \sim \pm\frac{\delta}{\Delta}k_0\phi_0\left(-\frac{256\pi^4 + 320\pi^2 m^2 + 64m^4}{9m^4}\right)^{1/2}, \tag{A 15}$$

regardless of the value of α chosen. The leading-order terms here are imaginary, which means that these solution branches must then have real part smaller than $O(\delta/\Delta)$. This is consistent with figure 2.

Appendix B. Numerical validation and sensitivity testing

B.1. *Implementation*

The dimensionless system (2.12)–(2.15) was written in streamfunction form as

$$\nabla\cdot\left[\left(1+\frac{\phi'}{\phi_0}\right)^{-2}\nabla\psi'\right]=-\mathscr{R}_C\frac{\partial C'}{\partial x}, \tag{B 1}$$

$$\left(1+\frac{\phi'}{\phi_0}\right)\frac{\partial C'}{\partial t}+\frac{\partial\psi'}{\partial x}+\left(\frac{\partial\psi'}{\partial x}\frac{\partial C'}{\partial z}-\frac{\partial\psi'}{\partial z}\frac{\partial C'}{\partial x}\right)=(\phi_0+\phi')\nabla^2C'$$
$$+\frac{\partial\phi'}{\partial z}+\left(\frac{\partial\phi'}{\partial x}\frac{\partial C'}{\partial x}+\frac{\partial\phi'}{\partial z}\frac{\partial C'}{\partial z}\right)-k_0\left(1+\frac{\phi'}{\phi_0}\right)\frac{(1-(\phi_0+\phi'))}{(1-\phi_0)}C', \tag{B 2}$$

$$\frac{\partial\phi'}{\partial t}=-\delta k_0(\phi_0+\phi')\frac{(1-(\phi_0+\phi'))}{(1-\phi_0)}C', \tag{B 3}$$

where $u'=-\partial\psi'/\partial z$ and $w'=\partial\psi'/\partial x$. This formulation eliminates the need to include pressure and impose continuity and makes the numerical integration significantly easier. The corresponding form of the boundary conditions (3.6) is

$$\frac{\partial\psi'}{\partial x}=0 \quad\text{and}\quad C'=0 \quad\text{at}\quad z=0 \quad\text{and}\quad z=1. \tag{B 4}$$

This system was integrated using the finite element package Comsol Multiphysics v3.5a. Numerical experiments were conducted both with zero initial conditions and with initial conditions into which a small periodic perturbation had been introduced,

$$C'(x,z,0)=z(1-z)\epsilon\sin(\pi x), \quad \phi(x,z,0)=\phi_0+0.01z(1-z)\sin(\pi x), \tag{B 5}$$

where $\epsilon=10^{-3}$. There was no perceptible difference between the results for the two cases.

B.2. *Validation*

The overall performance of the model was verified both for convection with no reaction or porosity evolution and for convection with a reaction but no porosity evolution. In both cases, the model reproduced the linear stability results found in § 3; details are given in § 4.1.

In order to check the convergence of our numerical model, simulations for $0\leqslant t\leqslant 5000$ were conducted using two different reaction rates, $k_0=0$ and $k_0=10$, and four different Rayleigh numbers: the critical Rayleigh number given by (3.26), and 10 %, 20 % and 50 % above this value. Each simulation was conducted using 4480 triangular mesh elements; absolute tolerances were varied between 10^{-3} and 10^{-6} while relative tolerances were varied between 10^{-2} and 10^{-5}. For each simulation, we noted the values for the maximum and minimum porosity ϕ, the maximum and minimum concentration perturbation C', and the maximum absolute velocity $|\boldsymbol{u}|$ over all time steps; we also plotted the maximum absolute velocity against time for each set of tolerances to check for convergence over all time steps. A relative tolerance of 10^{-3} and an absolute tolerance of 10^{-4} were found to give convergence of all key quantities to four significant figures while maintaining a reasonable solution time.

The mesh independence of the numerical method was tested similarly by conducting simulations with 1120, 4480, 17 920 and 71 680 triangular mesh elements and using the same reaction rates and Rayleigh numbers as used for the tolerance testing. Each simulation lasted 5000 time units and used a relative tolerance of 10^{-3} and an absolute tolerance of 10^{-4}. The same metrics as before were used to assess convergence.

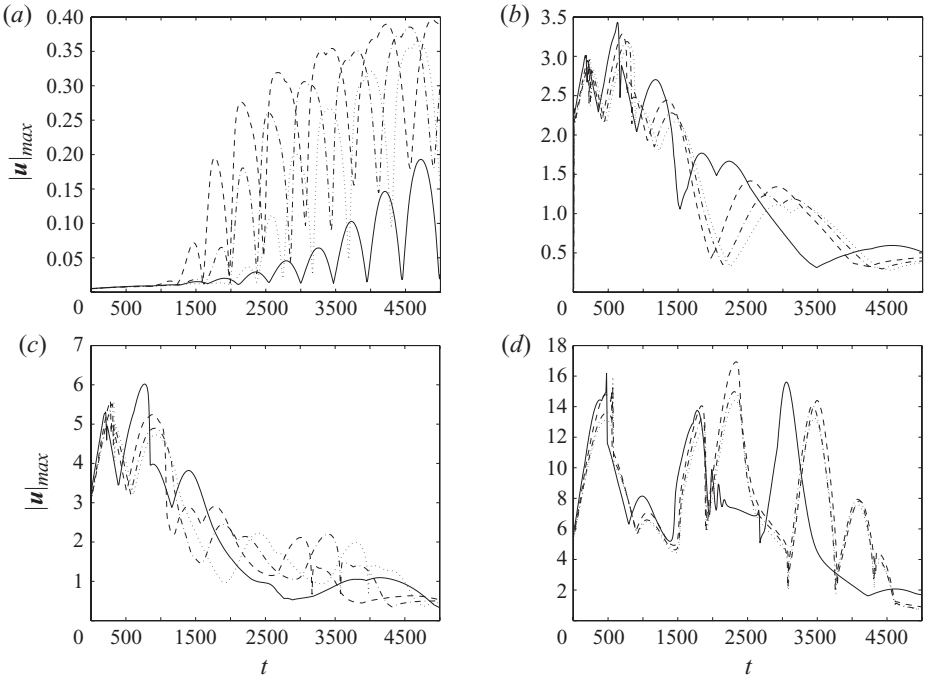

FIGURE 15. Maximum $|\boldsymbol{u}|$ throughout the whole domain when $k_0 = 10$ for (*a*) $\mathscr{R}_C = \mathscr{R}_{C,0}^{crit}$, (*b*) $\mathscr{R}_C = 1.1\mathscr{R}_{C,0}^{crit}$, (*c*) $\mathscr{R}_C = 1.2\mathscr{R}_{C,0}^{crit}$ and (*d*) $\mathscr{R}_C = 1.5\mathscr{R}_{C,0}^{crit}$. Lines represent solutions with different mesh elements: solid line, 1120; dashed line, 4480; dash-dotted line, 17 920; dotted line, 71 680 mesh elements.

When no reaction occurred ($k_0 = 0$), the solution was essentially mesh-independent; steady convection developed when the Rayleigh number was above the threshold $R_{C,0}^{crit}$, and all key quantities converged to three significant figures as long as at least 4480 mesh elements were employed.

The mesh-dependence at higher reaction rates is more subtle, as illustrated in figure 15. It is apparent from this that 1120 mesh elements are insufficient to resolve the behaviour consistently, whereas for 4480 or more mesh elements the evolution is qualitatively similar. However, particularly for the convective cases with Rayleigh numbers 10 %, 20 % and 50 % above the critical value, increasing the number of mesh elements results in the porosity evolving for longer before the first phase shift, signified by the reversal in porosity evolution. We also see that the maximum absolute velocity behaves in a similar way when we use at least 4480 mesh elements (figure 15). As the number of mesh elements is increased, the resolution of the numerical solution is increased and less numerical noise is encountered. Therefore, the porosity evolution can continue for longer before triggering an instability in the form of a phase shift. Since each solution displayed the same behaviour when at least 4480 elements were used, we concluded that 4480 elements were sufficient for mesh independence. However, it is important to note that the inception of the secondary instability is sensitive to the amount of numerical error introduced into the system.

REFERENCES

ANDERSON, D. M. & WORSTER, M. G. 1996 A new oscillatory instability in a mushy layer during the solidification of binary alloys. *J. Fluid Mech.* **307**, 245–267.

Bdzil, J. B. & Frisch, H. L. 1971 Chemical instabilities. II. Chemical surface reactions and hydrodynamic instability. *Phys. Fluids* **14** (3), 475–482.

Bdzil, J. B. & Frisch, H. L. 1980 Chemically driven convection. *J. Chem. Phys.* **72** (3), 1875–1886.

Bolton, E. W., Lasaga, A. C. & Rye, D. M. 1996 A model for the kinetic control of quartz dissolution and precipitation in porous media flow with spatially variable permeability: formulation and examples of thermal convection. *J. Geophys. Res.* **101** (B10), 22157–22187.

Bolton, E. W., Lasaga, A. C. & Rye, D. M. 1997 Dissolution and precipitation via forced-flux injection in a porous medium with spatially variable permeability: kinetic control in two dimensions. *J. Geophys. Res.* **102** (B6), 12159–12171.

Bolton, E. W., Lasaga, A. C. & Rye, D. M. 1999 Long-term flow/chemistry feedback in a porous medium with heterogenous permeability: kinetic control of dissolution and precipitation. *Am. J. Sci.* **299**, 1–68.

Chadam, J., Hoff, D., Merino, E., Ortoleva, P. & Sen, A. 1986 Reactive infiltration instabilities. *IMA J. Appl. Math.* **36**, 207–221.

Chadam, J., Ortoleva, P., Qin, Y. & Stamicar, R. 2001 The effect of hydrodynamic dispersion on reactive flows in porous media. *Eur. J. Appl. Maths* **12**, 557–569.

Chandrasekhar, S. 1961 *Hydrodynamic and Hydromagnetic Stability*. Oxford University Press.

Cochepin, B., Trotignon, L., Bildstein, O., Steefel, C. I., Lagneau, V. & Van der lee, J. 2008 Approaches to modelling coupled flow and reaction in a 2D cementation experiment. *Adv. Water Resour.* **31**, 1540–1551.

Daccord, G. 1987 Chemical dissolution of a porous medium by a reactive fluid. *Phys. Rev. Lett.* **58**, 479–482.

Ennis-King, J. & Paterson, L. 2007 Coupling of geochemical reactions and convective mixing in the long-term geological storage of carbon dioxide. *Intl J. Greenh. Gas Control* **1**, 86–93.

Gatica, J. E., Viljoen, H. J. & Hlavacek, V. 1989 Interaction between chemical reaction and natural convection in porous media. *Chem. Engng Sci.* **44** (9), 1853–1870.

Gilman, A. & Bear, J. 1994 The influence of free convection on soil salinization in arid regions. *Transp. Porous Med.* **23**, 275–301.

Gutkowicz-Krusin, D. & Ross, J. 1980 Rayleigh–Bénard instability in reactive binary fluids. *J. Chem. Phys.* **72** (6), 3577–3587.

Hallworth, M. A., Huppert, H. E. & Woods, A. W. 2005 Dissolution-driven convection in a reactive porous medium. *J. Fluid Mech.* **535**, 255–285.

Hinch, E. J. & Bhatt, B. S. 1990 Stability of an acid front moving through porous media. *J. Fluid Mech.* **212**, 279–288.

Hoefner, M. L. & Fogler, H. S. 1988 Pore evolution and channel formation during flow and reaction in porous media. *AIChE J.* **34** (1), 45–54.

Horton, C. W. & Rogers, F. T. 1945 Convection currents in a porous medium. *J. Appl. Phys.* **16**, 367–370.

Kaufman, J. 1994 Numerical models of fluid flow in carbonate platforms: implications for dolomitization. *J. Sedim. Res.* A **64**, 128–139.

Lapwood, E. R. 1948 Convection of a fluid in a porous medium. *Proc. Camb. Phil. Soc.* **44**, 508–521.

Lowell, R. P., Cappellen, P. V. & Germanovitch, L. N. 1993 Silica precipitation in fractures and the evolution of permeability in hydrothermal upflow zones. *Science* **260** (5105), 192–194.

Mamou, M. & Vasseur, P. 1999 Thermosolutal bifurcation phenomena in porous enclosures subject to vertical temperature and concentration gradients. *J. Fluid Mech.* **395**, 61–87.

Mamou, M., Vasseur, P. & Hasnaoui, M. 2001 On numerical stability analysis of double-diffusive convection in confined enclosures. *J. Fluid Mech.* **433**, 209–250.

Nield, D. A. & Bejan, A. 2006 *Convection in Porous Media*, 3rd edn. Springer.

Oldenburg, C. M. & Pruess, K. 1998 Layered thermohaline convection in hypersaline geothermal systems. *Transp. Porous Med.* **33**, 29–63.

Phillips, O. M. 1991 *Flow and Reactions in Permeable Rocks.* Cambridge University Press.

Phillips, O. M. 2009 *Geological Fluid Dynamics: Sub-Surface Flow and Reactions.* Cambridge University Press.

Pritchard, D. & Richardson, C. N. 2007 The effect of temperature-dependent solubility on the onset of thermosolutal convection in a horizontal porous layer. *J. Fluid Mech.* **571**, 59–95.

Raffensperger, J. P. & Garven, G. 1995*a* The formation of unconformity-type uranium ore deposits. 1. Coupled groundwater flow and heat transport modelling. *Am. J. Sci.* **295** (5), 581–636.

Raffensperger, J. P. & Garven, G. 1995*b* The formation of unconformity-type uranium ore deposits. 2. Coupled hydrochemical modelling. *Am. J. Sci.* **295** (6), 639–696.

Raw, A. W. V. & Woods, A. W. 2003 On gravity-driven flow through a reacting porous rock. *J. Fluid Mech.* **474**, 227–243.

Rudraiah, N., Srimani, P. & Friedrich, R. 1982 Finite amplitude convection in a two-component fluid saturated porous layer. *Intl J. Heat Mass Transfer* **25** (5), 715–722.

Sharp, J. M. & Shi, M. 2009 Heterogeneity effects on possible salinity-driven free convection in low-permeability strata. *Geofluids* **9**, 263–274.

Steinberg, V. & Brand, H. 1983 Convective instabilities of binary mixtures with fast chemical reaction in a porous medium. *J. Chem. Phys.* **78** (5), 2655–2660.

Steinberg, V. & Brand, H. 1984 Amplitude equations for the onset of convection in a reactive mixture in a porous medium. *J. Chem. Phys.* **80** (1), 431–435.

Stevens, J. D., Sharp, J. M., Simmons, C. T. & Fenstemaker, T. R. 2009 Evidence of free convection in groundwater: field-based measurements beneath wind-tidal flats. *J. Hydrology* **375**, 394–409.

Verdon, J. & Woods, A. W. 2007 Gravity-driven reacting flows in a confined porous aquifer. *J. Fluid Mech.* **588**, 29–41.

Viljoen, H. J., Gatica, J. E. & Hlavacek, V. 1990 Bifurcation analysis of chemically driven convection. *Chem. Engng Sci.* **45** (2), 503–517.

Wollkind, D. J. & Frisch, H. L. 1971 Chemical instabilities. I. A heated horizontal layer of dissociating fluid. *Phys. Fluids* **14** (1), 13–18.

Wooding, R. A., Tyler, S. W. & White, I. 1997 Convection in groundwater below an evaporating salt lake. 1. Onset of instability. *Water Resour. Res.* **33** (6), 1199–1217.

Worster, M. G. 1997 Convection in mushy layers. *Annu. Rev. Fluid Mech.* **29**, 91–122.

Zhao, C., Hobbs, B. E., Ord, A., Hornby, P. & Peng, S. 2008 Morphological evolution of three-dimensional chemical dissolution front in fluid-saturated porous media: a numerical simulation approach. *Geofluids* **8**, 113–127.